The Astrophysical Journal Supplement Series, 164:280–296, 2006 May

ELECTRON-ION RECOMBINATION RATE COEFFICIENTS AND PHOTOIONIZATION CROSS SECTIONS FOR ASTROPHYSICALLY ABUNDANT ELEMENTS. XI. N V–VI AND F VII–VIII FOR ULTRAVIOLET AND X-RAY MODELING

Sultana N. Nahar
Department of Astronomy, Ohio State University, Columbus, OH 43210; nahar@astronomy.ohio-state.edu
Received 2005 November 15; accepted 2006 January 19

ABSTRACT

The inverse processes of photoionization and electron-ion recombination for $h\nu + \text{N V} \leftrightarrow \text{N VI} + e$, $h\nu + \text{N VI} \leftrightarrow \text{N VII} + e$, $h\nu + \text{F VII} \leftrightarrow \text{F VIII} + e$, and $h\nu + \text{F VIII} \leftrightarrow \text{F IX} + e$ are studied in detail using a self-consistent unified method for the total electron-ion recombination. The method enables calculation of the total and level-specific recombination rate coefficients α_R and $\alpha_R(i)$, subsuming both radiative and dielectronic recombination (RR and DR). The photoionization and recombination cross sections $\sigma_{\rm PI}$ and $\sigma_{\rm RC}$ are computed using an identical wave function expansion for both processes in the close coupling approximation using the ***R***-matrix method. The results include total and partial photoionization cross sections and recombination rate coefficients for all fine-structure levels up to $n \leq 10$, about 100 for Li-like N V and F VII with $1/2 \leq J \leq 17/2$, and over 170 for He-like N VI and F VIII with $0 \leq J \leq 10$. Level-specific $\sigma_{\rm PI}(nSLJ)$ and $\alpha_R(T; nSLJ)$ are calculated for the first time for these ions. The coupled-channel wave function expansions for N V and F VII consist of 17 levels of cores N VI and F VIII, respectively, and for N VI and F VIII consist of 16 levels of cores N VII and F IX, respectively. Relativistic fine structure is considered through the Breit-Pauli ***R***-matrix method. The single-valued total $\alpha_R(T)$ is presented over an extended temperature range for astrophysical and laboratory plasma applications. Although the total unified $\alpha_R(T)$ for all ions agree well with the available published RR+DR rates, significant differences are noted at the DR peak for N V. Total $\sigma_{\rm RC}(E)$ and $\alpha_R(E)$ as functions of photoelectron energy are presented for comparison with experiments. Total rates for H-like N VII and F IX are also given for completeness. The cross sections $\sigma_{\rm PI}$ and $\sigma_{\rm RC}$ include important atomic effects such as radiation damping, channel couplings, and interference of DR and RR, and should be accurate to within 10%–15%. The comprehensive data sets are applicable for ionization balance and recombination-cascade models for UV and X-ray lines.

Subject headings: atomic data — atomic processes — line: formation — X-rays: general

1. INTRODUCTION

X-ray and ultraviolet emission/absorption of He- and Li-like ions provide powerful diagnostics of physical conditions and chemical composition in hot astrophysical and laboratory plasmas (e.g., Gabriel & Jordan 1969; Leighly et al. 1997; Lee et al. 2001; Ness et al. 2003; Hillier 2005). For example, the distinct spectral Kα lines involving transitions between the $n = 2$ and 1 levels of a He-like ion are used for the determination of the temperature, density, and ionization state of the plasma (e.g., Oelgoetz & Pradhan 2001, 2004). These lines in astrophysical spectra are generated mainly by all elements from carbon to iron. The UV lines have been used for velocities and column densities of a variety of ions (e.g., Fitzpatrick & Spitzer 1997). Astrophysical models require accurate parameters for the atomic processes for proper analysis. The determination of the ionic abundances in a source requires the knowledge of ionization and electron-ion recombination rates for the He-like ionization stage and adjacent Li-like and H-like stages.

The UV resonance doublet in Li-like ions such as C IV, N V, and O VI (Dopita & Sutherland 2003) is a prominent example of line formation dependent on temperature, column density, and velocity fields in the source. In N V, one of the ions considered in the present work, the fine-structure doublet occurs at $\lambda\lambda$1239, 1243 due to the dipole allowed transitions $1s^2 2p(^2P^o_{1/2,\,3/2}) \rightarrow 1s^2 2s(^2S_{1/2})$. The proximity of these N V lines to Lyα (1215 Å) may also be noted, and thereby the possibility of Lyα fluorescence (Dopita & Sutherland 2003; see their Fig. 4.11). In addition to collisional and fluorescent excitation, emission lines in general may contain a component due to (electron+ion) recombination, particularly in transient (e.g., shocked) plasmas out of ionization equilibrium. In order to model the recombination component, recombination-cascade coefficients are needed, which in turn require level-specific recombination rate coefficients for a large number of excited levels.

As part of the present series of papers, highly detailed and comprehensive studies of level-specific and total cross sections and rates using a self-consistent unified treatment are reported for the Li- and He-like ionization stages of various astrophysically abundant elements: C IV and C V (Nahar et al. 2000), O VI and O VII (Nahar & Pradhan 2003), Ne VIII and Ne IX (Nahar & Pradhan 2006), Fe XXV and Fe XXV (Nahar et al. 2001), and Ni XXVI and Ni XXVII (Nahar 2005). The unified method for total electron-ion recombination accounts for both radiative and dielectronic recombination processes in an ab initio manner and provides a single set of recombination rate coefficients. Futhermore, photoionization and recombination cross sections are computed self-consistently using the same wave function expansion. The present work reports on the ions N V, N VI, F VII, and F VIII, completing the sequence between carbon and neon as reported in earlier work. We also contrast and compare with nonrelativistic photoionization and recombination calculations for N V and N VI in *LS* coupling (Nahar & Pradhan 1997). The present calculations include relativistic fine structure and the radiation damping of low-lying resonances (important for Li- and He-like ions) with highly resolved cross sections.

Level-specific recombination rate coefficients α_i for each ion are presented for all levels ($nSLJ$, $n \leq 10$). Calculations of recombination-cascade contributions for important lines require

accurate atomic parameters for fine-structure levels up to fairly high n levels, as presented in this report.

The results should be useful for spectral analysis of X-ray observations from the *Chandra X-Ray Observatory* and *XMM-Newton* and UV observations from the *Far Ultraviolet Spectroscopic Explorer* (*FUSE*) and other UV satellites, such as the *Solar and Heliospheric Observatory* (*SOHO*). The data are presented at all energies and temperatures prevalent in high-temperature sources such as active galactic nuclei, supernova remnants, and hot stellar coronae (e.g., Canizares et al. 2000).

2. THEORY

The inverse processes of photoionization and electron-ion recombination may occur as

$$e + \mathrm{X}^{++} \leftrightarrow h\nu + \mathrm{X}^{+}, \tag{1}$$

where the right arrow indicates the direct or radiative recombination (RR) and the left arrow indicates photoionization, or through an intermediate doubly excited autoionizing state as

$$e + \mathrm{X}^{++} \leftrightarrow (\mathrm{X}^{+})^{**} \leftrightarrow \begin{cases} e + \mathrm{X}^{++} & \text{(AI)}, \\ h\nu + \mathrm{X}^{+} & \text{(DR)}, \end{cases} \tag{2}$$

where the autoionizing state leads either to autoionization (AI) or to dielectronic recombination (DR) via radiation damping. The inverse of DR is autoionization, through an autoionizing state that appears as a resonance in photoionization cross sections. RR and DR are inseparable in nature, and usually combined (added) together in practical applications. The unified method subsumes both the RR and DR processes and considers photoionization from and recombination into the infinity of levels of the (e + ion) system in an ab initio manner in the close coupling (CC) approximation (Nahar & Pradhan 1992, 1994; Nahar 1996), as briefly outlined below. The present calculations include relativistic effects in the Breit-Pauli approximation and radiation damping of low-n resonances, which is usually significant for Li- and He-like ions, with radiative decay rates in the core ion comparable to autoionization rates (Zhang et al. 1999).

In the CC approximation the target (core) is represented by an N-electron system and the $(N + 1)$th electron as the freely interacting electron. The total wave function $\Psi(E)$ of the $(N + 1)$th electron+ion system of symmetry $J\pi$ is represented by an expansion of target eigenfunctions χ_i as

$$\Psi(\mathrm{ion} + e;\ E) = A \sum_i \chi_i(\mathrm{ion})\theta_i + \sum_j c_j \Phi_j(\mathrm{ion} + e), \tag{3}$$

where the target is a specific level $J_i\pi_i$. Here θ_i is the wave function of the $(N + 1)$th electron in a channel $S_iL_i(J_i)\pi_i k_i^2 l(J\pi)$, and k_i^2 is its incident kinetic energy. A channel is open or closed depending on positive or negative energy. The autoionizing resonances result from the couplings of open and closed channels. The Φ_j are correlation functions of the $(N + 1)$-electron system and account for short-range correlations and orthogonality between continuum and bound orbitals.

The relativistic Hamiltonian, as adopted in the Breit-Pauli $\boldsymbol{R}$-matrix (BPRM) method under the Iron Project (Hummer et al. 1993), is

$$H_{N+1}^{\mathrm{BP}} = H_{N+1}^{\mathrm{NR}} + H_{N+1}^{\mathrm{mass}} + H_{N+1}^{\mathrm{Dar}} + H_{N+1}^{\mathrm{so}}, \tag{4}$$

where the first term, H_{N+1}^{NR}, is the nonrelativistic Hamiltonian, and the additional one-body terms are the mass correction term, H_{N+1}^{mass}, the Darwin term, H_{N+1}^{Dar}, and the spin-orbit interaction term, H_{N+1}^{so}. The set of $SL\pi$ is recoupled for $J\pi$ levels of the (e + ion) system, which is followed by diagonalization of the Hamiltonian, $H_{N+1}^{\mathrm{BP}}\Psi = E\Psi$. The positive and negative energies of equation (4) define the continuum ($E = k^2 \geq 0$), Ψ_F, or bound ($E < 0$), Ψ_B, states.

The reduced matrix element for the bound-free transition is $\langle \Psi_B \| \boldsymbol{D} \| \Psi_F \rangle$, where $\boldsymbol{D}$ is the dipole operator; $\boldsymbol{D}_L = \sum_i r_i$ in length form, where the sum is the number of electrons. The dipole line strength, $\boldsymbol{S} = |\langle \Psi_B \| \boldsymbol{D} \| \Psi_F \rangle|^2$, gives the photoionization cross section, $\sigma_{\mathrm{PI}} = [4\pi^2/(3g_i c)]\omega \boldsymbol{S}$, where g_i is the statistical weight factor of the initial bound state. For the present H- and the He-like recombining ions, the radiative decay rates A_r for transitions $2p(^2P^o_{3/2,\,1/2}) \rightarrow 1s(^2S_{1/2})$ and $1s2p(^1P^o_1) \rightarrow 1s^2(^1S_0)$ are comparable to that of autoionization (typically $A_a \sim 10^{12}$–10^{14} s^{-1}), as seen in Table 3, and the autoionizing resonances can radiatively damp to a significant extent. The radiative damping effect of all resonances, up to effective quantum number $\nu \leq 10$, are considered using a resonance fitting procedure (Sakimoto et al. 1990; Pradhan & Zhang 1997; Zhang et al. 1999).

The photorecombination cross section σ_{RC} is obtained from the photoionization cross section σ_{PI} through the principle of detailed balance (Milne relation),

$$\sigma_{\mathrm{RC}}(\epsilon) = \frac{\alpha^2}{4}\frac{g_i}{g_j}\frac{(\epsilon + I)^2}{\epsilon}\sigma_{\mathrm{PI}}, \tag{5}$$

in rydbergs; α is the fine-structure constant, ϵ is the photoelectron energy, g_j is the statistical weight factor of the recombined ion, and I is the ionization potential. The cross section σ_{RC} computed from σ_{PI} with a sufficiently large number of energies to delineate the nonresonant background and the autoionizing resonances represents both RR and DR processes. Assuming that the recombining ion is in the ground state, the above equation represents the partial photoionization cross sections, leaving the ion in the ground state. Recombination rate coefficients of individual recombined levels are obtained by convolving σ_{RC} over Maxwellian electron distribution $f(v)$ at a given temperature:

$$\alpha_{\mathrm{RC}}(T) = \int_0^\infty v f(v) \sigma_{\mathrm{RC}}\, dv. \tag{6}$$

Contributions from the bound levels are added for the total recombination rate coefficient α_{RC} and for the total recombination cross sections σ_{RC}.

The recombination can take place into the ground or any of the excited recombined (e + ion) states. The unified method divides the recombined levels into two groups: group A with $n \leq n_0$ and all possible fine-structure $J\pi$ symmetries, and group B with $n_0 < n \leq \infty$, where n_0 is typically 10. Individual σ_{PI}, σ_{RC}, and α_R are obtained for all possible bound levels with $n \leq n_0 \sim 10$ (group A) in the CC approximation as described above.

Group B levels, $n_0 < n \leq \infty$, are treated through quantum defect theory of DR within the CC approximation (Bell & Seaton 1985; Nahar & Pradhan 1992, 1994). The background contribution of these levels is negligible except at very low temperature, and DR is dominant in the region below the threshold of convergence for high-n resonances. To each excited threshold of the core, $J_i\pi_i$, belongs an infinite series of $(N + 1)$ electron levels, $J_i\pi_i\nu l$, to which recombination can occur. The high-ν levels are dominated by DR. The contributions from these levels are obtained from the DR collision strengths, $\Omega(\mathrm{DR})$, using radiation damping theory (Bell & Seaton 1985; Nahar & Pradhan 1994):

$$\Omega(\mathrm{DR}) = \sum_{SL\pi} \sum_n (1/2)(2S + 1)(2L + 1) P_n^{SL\pi}(\mathrm{DR}), \tag{7}$$

TABLE 1

TARGET LEVELS IN THE EIGENFUNCTION EXPANSIONS OF N V AND N VI

	N VI		N VII	
NUMBER	Level	E_t (ryd)	Level	E_t (ryd)
1.....	$1s^2(^1S_0)$	0.0	$1s(^2S_{1/2})$	0.0
2.....	$1s2s(^3S_1)$	30.855	$2p(^2P^o_{1/2})$	36.7674
3.....	$1s2p(^3P^o_0)$	31.332	$2s(^2S_{1/2})$	36.7679
4.....	$1s2p(^3P^o_1)$	31.332	$2p(^2P^o_{3/2})$	36.7755
5.....	$1s2p(^3P^o_2)$	31.335	$3p(^2P^o_{1/2})$	43.5792
6.....	$1s2s(^1S_0)$	31.341	$3s(^2S_{1/2})$	43.5793
7.....	$1s2p(^1P^o_1)$	31.656	$3d(^2D_{3/2})$	43.5816
8.....	$1s3s(^3S_1)$	36.377	$3p(^2P^o_{3/2})$	43.5816
9.....	$1s3s(^1S_0)$	36.505	$3d(^2D_{5/2})$	43.5824
10.....	$1s3p(^3P^o_2)$	36.507	$4p(^2P^o_{1/2})$	45.9630
11.....	$1s3p(^3P^o_1)$	36.507	$4s(^2S_{1/2})$	45.9630
12.....	$1s3p(^3P^o_0)$	36.507	$4d(^2D_{3/2})$	45.9640
13.....	$1s3d(^1D_3)$	36.573	$4p(^2P^o_{3/2})$	45.9640
14.....	$1s3d(^3D_2)$	36.573	$4f(^2F^o_{5/2})$	45.9643
15.....	$1s3d(^3D_1)$	36.573	$4d(^2D_{5/2})$	45.9643
16.....	$1s3d(^1D_2)$	36.576	$4f(^2F^o_{7/2})$	45.9645
17.....	$1s3p(^1P^o_1)$	36.600		

NOTES.—N VI, correlations: $2s^2$, $2p^2$, $3s^2$, $3p^2$, $3d^2$, $2s2p$, $2s3s$, $2s3p$, $2s3d$, $2s4s$, $2s4p$, $2p3s$, $2p3p$, $2p3d$, $2p4s$, $2p4p$. N VI, λ_{nl}: 0.991 (1*s*), 991 (2*s*), 0.775 (2*p*), 1.16883 (3*s*), 0.91077 (3*p*), 1.0075 (3*d*), 1 (4*s*), 1 (4*p*).

where the DR probability $P_n^{SL\pi}$ in entrance channel n is $P_n^{SL\pi}(\mathrm{DR}) = (1 - \boldsymbol{S}_{ee}^{\dagger}\boldsymbol{S}_{ee})_n$. Here $\boldsymbol{S}_{ee}$ is the matrix for electron scattering *including* radiation damping. The recombination cross section σ_{RC} in megabarns (Mbarn) is related to the collision strength Ω_{RC} as

$$\sigma_{\mathrm{RC}}(i \rightarrow j)\,(\mathrm{Mbarn}) = \frac{\pi\Omega_{\mathrm{RC}}(i,\ j)}{(g_i k_i^2)(a_0^2/1.0\times10^{-18})}, \qquad (8)$$

where k_i^2 is in rydbergs. Since σ_{RC} diverges at zero photoelectron energy, the total collision strength Ω is used in the recombination

TABLE 2

TARGET LEVELS IN THE EIGENFUNCTION EXPANSIONS OF F VII AND F VIII

	F VIII		F IX	
NUMBER	Level	E_t (ryd)	Level	E_t (ryd)
1.....	$1s^2(^1S_0)$	0.0	$1s(^2S_{1/2})$	0.00
2.....	$1s2s(^3S_1)$	53.12724	$2p(^2P^o_{1/2})$	60.8008
3.....	$1s2p(^3P^o_0)$	53.77023	$2s(^2S_{1/2})$	60.8019
4.....	$1s2p(^3P^o_1)$	53.77159	$2p(^2P^o_{3/2})$	60.8228
5.....	$1s2p(^3P^o_2)$	53.78025	$3p(^2P^o_{1/2})$	72.0682
6.....	$1s2s(^1S_0)$	53.79301	$3s(^2S_{1/2})$	72.0685
7.....	$1s2p(^1P^o_1)$	54.21948	$3d(^2D_{3/2})$	72.0746
8.....	$1s3s(^3S_1)$	62.74156	$3p(^2P^o_{3/2})$	72.0746
9.....	$1s3p(^3P^o_0)$	62.90076	$3d(^2D_{5/2})$	72.0768
10.....	$1s3p(^3P^o_1)$	62.90076	$4p(^2P^o_{1/2})$	76.0108
11.....	$1s3p(^3P^o_2)$	62.90076	$4s(^2S_{1/2})$	76.0109
12.....	$1s3s(^1S_0)$	62.90723	$4d(^2D_{3/2})$	76.0136
13.....	$1s3d(^1D_1)$	62.99526	$4p(^2P^o_{3/2})$	76.0136
14.....	$1s3d(^3D_2)$	62.99526	$4f(^2F^o_{5/2})$	76.0145
15.....	$1s3d(^3D_3)$	63.01312	$4d(^2D_{5/2})$	76.0145
16.....	$1s3d(^1D_2)$	63.02232	$4f(^2F^o_{7/2})$	76.0149
17.....	$1s3p(^1P^o_1)$	63.02861		

NOTES.—F VIII, correlations: $2s^2$, $2p^2$, $3s^2$, $3p^2$, $3d^2$, $2s2p$, $2s3s$, $2s3p$, $2s3d$, $2s4s$, $2s4p$, $2p3s$, $2p3p$, $2p3d$, $2p4s$, $2p4p$. F VIII, λ_{nl}: 1.1 (1*s*), 0.99 (2*s*), 1 (2*p*), 1 (3*s*), 1 (3*p*), 1 (3*d*), 1 (4*s*), 1 (4*p*).

TABLE 3

RADIATIVE DECAY RATES A_{fi}

Target Level	A_{fi} (s^{-1})	Target Level	A_{fi} (s^{-1})
N VI, GD: $1s^2\ ^1S_0$			
$1s2p(^3P^o_1)$.....	1.02(8)	$1s3p(^3P^o_1)$.....	2.84(7)
$1s2p(^1P^o_1)$.....	1.89(12)	$1s3p(^1P^o_1)$.....	5.77(11)
N VII, GD: $1s\ ^2S^{1/2}$			
$2p(^2P^o_{1/2})$.....	1.50(12)	$3p(^2P^o_{3/2})$.....	4.00(11)
$2p(^2P^o_{3/2})$.....	1.50(12)	$4p(^2P^o_{1/2})$.....	1.61(11)
$3p(^2P^o_{1/2})$.....	3.99(11)	$4p(^2P^o_{3/2})$.....	1.62(11)
F VIII, GD: $1s^2\ ^1S_0$			
$1s2p(^3P^o_1)$.....	1.54(9)	$1s3p(^3P^o_1)$.....	4.36(8)
$1s2p(^1P^o_1)$.....	5.60(12)	$1s3p(^1P^o_1)$.....	1.63(12)
F IX, GD: $1s\ ^2S^{1/2}$			
$2p(^2P^o_{1/2})$.....	4.11(12)	$3p(^2P^o_{3/2})$.....	1.09(12)
$2p(^2P^o_{3/2})$.....	4.11(12)	$4p(^2P^o_{1/2})$.....	4.36(11)
$3p(^2P^o_{1/2})$.....	1.09(12)	$4p(^2P^o_{3/2})$.....	4.40(11)

NOTE.—Rates are for allowed transitions to the ground level (GD), which is $1s^2\ ^1S_0$ for N VI and F VIII, and $1s\ ^2S_{1/2}$ for N VII and F IX.

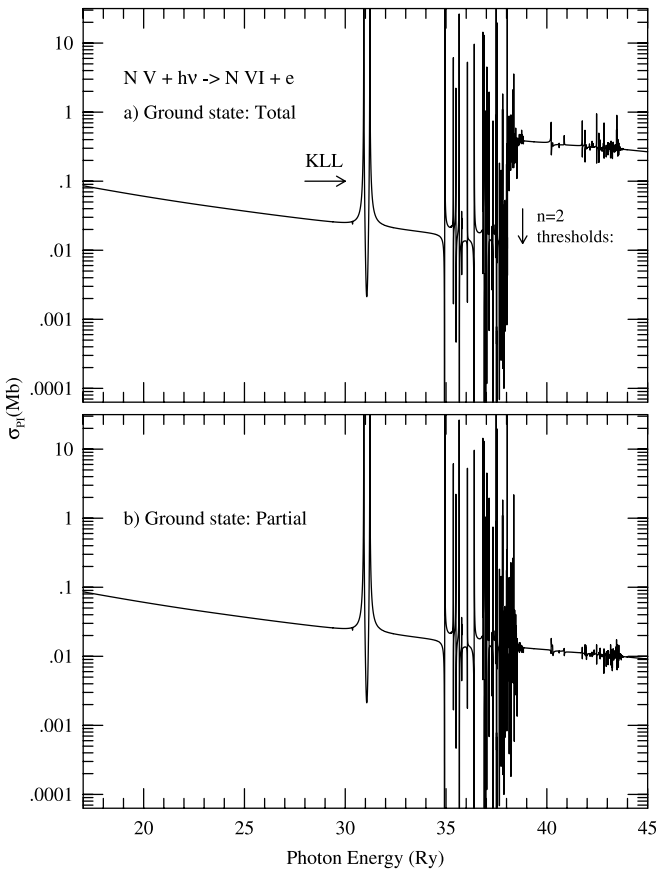

FIG. 1.—Photoionization cross sections σ_{PI} of the ground level $1s^2 2s\ (^2S_{1/2})$ of N V. (*a*) Total cross section; the large jump around the $n = 2$ thresholds ($\sim$38.8 ryd) is the K-shell ionization edge ($h\nu + 1s^2 2l \rightarrow 1s2l + e$). (*b*) Partial cross section for ionization into the ground level $1s^2\ (^1S_0)$ of core N VI; there is no jump in the partial cross section.

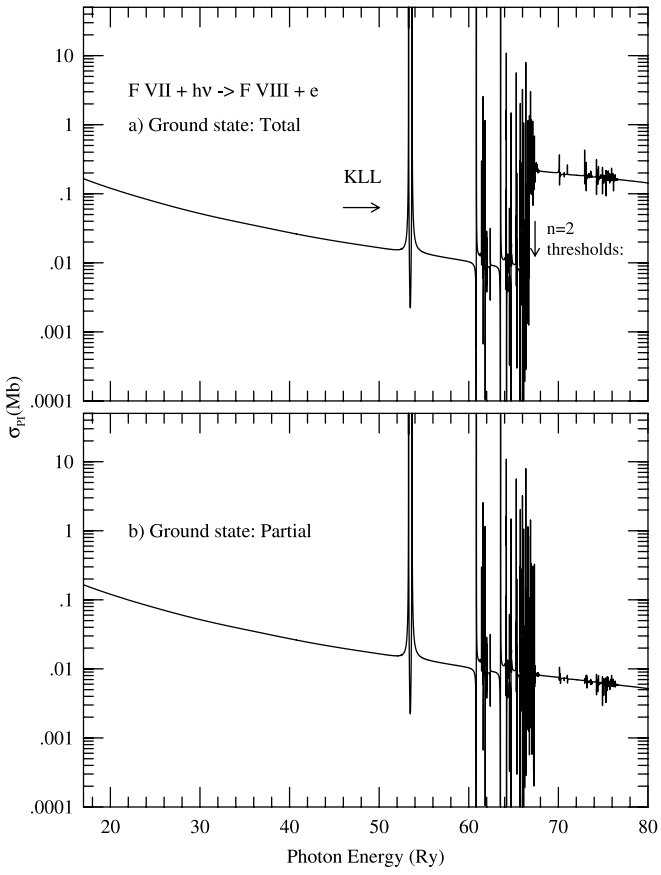

FIG. 2.—Photoionization cross sections σ_{PI} of the ground level $1s^2 2s\ (^2S_{1/2})$ of F VII. (*a*) Total cross section; the K-shell ionization jump around the $n = 2$ thresholds (~67.4 ryd) is due to $h\nu + 1s^2 2l \rightarrow 1s2l + e$. (*b*) Partial cross section for ionization into the ground level $1s^2\ (^1S_0)$ of core F VIII; there is no K-shell edge in the partial cross sections.

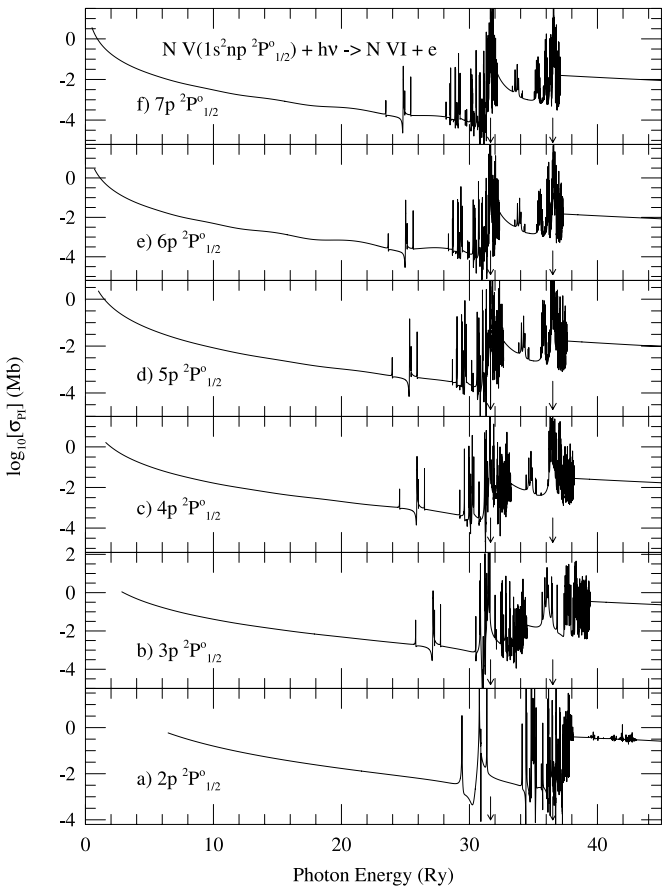

FIG. 3.—Photoionization cross sections of the Rydberg series of levels, $1s^2 np(^2P^o_{1/2})$ with $2 \leq n \leq 7$, of N V. Prominent PEC resonances are seen (indicated by arrows) at about 31.65 ryd due to the excited $n = 2$ core levels $1s2p\ ^3P^o_1,\ ^1P^o_1$ and at about 36.53 ryd due to the $n = 3$ core levels $1s3p\ ^3P^o_1,\ ^1P^o_1$.

rate calculations. The unified method is not restricted to $n = 10$. However, a detailed calculation of σ_{PI} of high-n levels is unnecessary since they approach hydrogenic behavior. Background photoionization cross sections for the high-n group B levels are computed hydrogenically, and the corresponding contribution to α_R is referred to as the "high-n top-up" contribution (Nahar 1996).

3. COMPUTATIONS

The calculations for photoionization and electron-ion recombination span a number of stages using the BPRM package of codes, with several other codes. The orbital wave functions of the core ion are obtained from configuration interaction atomic structure calculations using the code SUPERSTRUCTURE (Eissner et al. 1974). The BPRM calculations begin with these orbital wave functions.

The wave function expansions for the Li-like N V and F VII consist of 17 fine-structure levels of the *spectroscopic* configurations $1s^2$, $1s2s$, $1s2p$, $1s3s$, $1s3p$, and $1s3d$ of the target cores N VI and F VIII, respectively. The energy levels are given in Tables 1 and 2. The set of *correlation* configurations and the Thomas-Fermi scaling parameters for each orbital in the atomic structure calculations are also given in the tables. The energies are the observed values from the NIST Web site.[1] Although the corresponding calculated energies are very close to the observed values, the latter are used for more accurate resonance positions.

[1] See http://www.nist.gov.

The second term of the wave function in equation (3), representing bound-state correlation functions, includes all possible $(N + 1)$ particle configurations with 0 to maximum orbital occupancies of $2s^2$, $2p^2$, $3s^2$, $3p^2$, $3d^2$, $4s$, and $4p$ for both N V and F VII. The radial integrals for the partial wave expansion in equation (3) are specified for $0 \leq l \leq 9$, with an $\boldsymbol{R}$-matrix basis set of 40 continuum functions. Computations are carried out for all angular momenta $0 \leq L \leq 11$ and $1/2 \leq J \leq 17/2$.

The coupled-channel wave function expansion for both N VI and F VIII consists of 16 fine-structure levels of N VII and F IX of configurations $1s$, $2s$, $2p$, $3s$, $3p$, $3d$, $4s$, $4p$, $4d$, and $4f$. The orbital wave functions and level energies are given in Tables 1 and 2. The bound-state correlation functions include all possible configurations from 0 to maximum orbital occupancies of $1s^2$, $2s^2$, $2p^2$, $3s^2$, $3p^2$, $3d^2$, $4s^2$, $4p^2$, $4d$, and $4f$. The partial wave expansion includes all orbitals $0 \leq l \leq 9$, with an $\boldsymbol{R}$-matrix basis set of 30 continuum functions. Computations are carried out for all angular momenta $0 \leq L \leq 14$ and $0 \leq J \leq 10$ for the core.

Both the partial and the total photoionization cross sections are obtained for all bound levels using the BPRM $\boldsymbol{R}$-matrix codes (Berrington et al. 1995; Zhang et al. 1999). They are extensions of the Opacity Project codes (Berrington et al. 1987) to include the relativistic effects (Scott & Burke 1980; Scott & Taylor 1982). The energy levels are obtained from STGB and are identified using the code PRCBPID (Nahar & Pradhan 2000). Radiation damping of resonances up to $n = 10$ are included using the extended codes STGF and STGBF (Nahar & Pradhan 1994; Zhang et al. 1999). The narrow resonances of these ions were

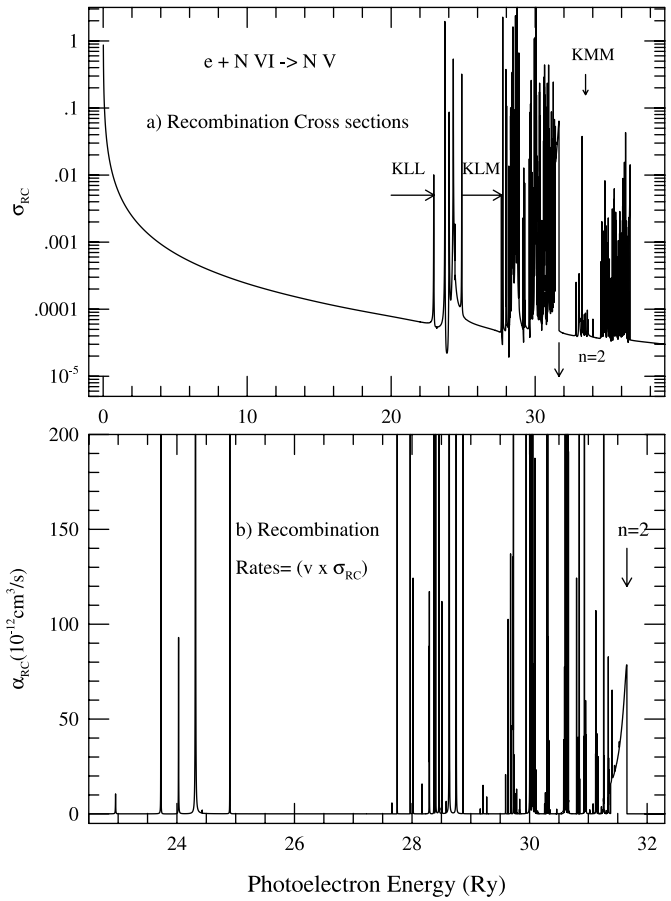

FIG. 4.—(*a*) Total unified (e + ion) recombination cross sections, $\sigma_{\rm RC}$, and (*b*) unified recombination rate coefficients, $\alpha_{\rm RC}(E)$, vs. photoelectron energy for e + N VI → N V. Separated resonance complexes KLL, KLM, etc., of the $n = 2$ and KMM, KMN, etc., of the $n = 3$ thresholds can be noted. The coefficient $\alpha_{\rm RC}(E)$, convolved with an energy bandwidth, is a measurable quantity.

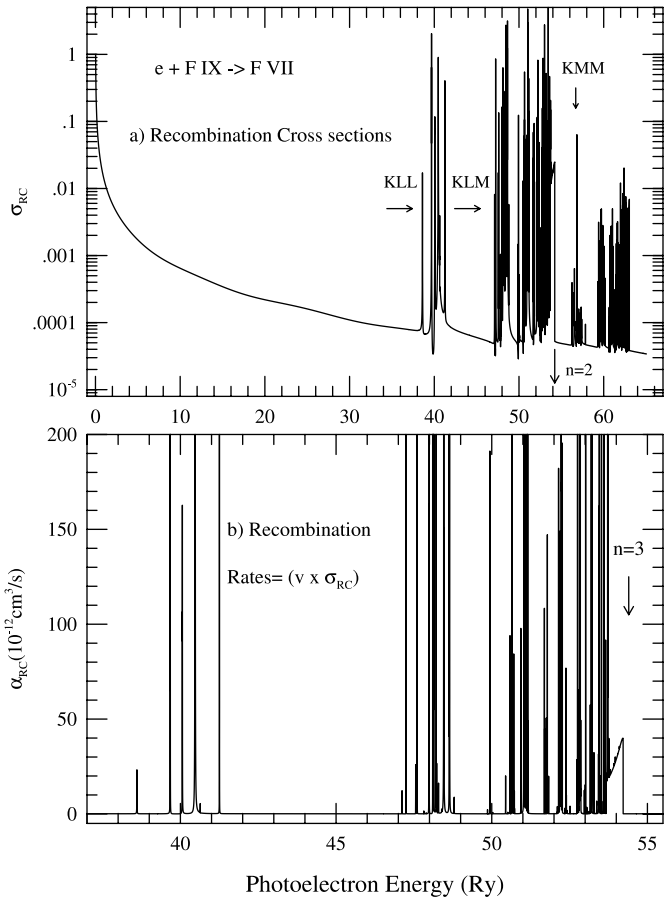

FIG. 5.—(*a*) Total unified (e + ion) recombination cross sections, $\sigma_{\rm RC}$, and (*b*) unified recombination rate coefficients, $\alpha_{\rm RC}(E)$, vs. photoelectron energy for e + F VIII → F VII. Separated resonance complexes KLL, KLM, etc., of the $n = 2$ and KMM, KMN, etc., of the $n = 3$ thresholds can be noted. The coefficient $\alpha_{\rm RC}(E)$, convolved with an energy bandwidth, is a measurable quantity.

delineated at a very fine energy mesh. The program PBPRAD extends the total photoionization cross sections in the high-energy region beyond the highest threshold in the target ion by a "tail" using a fitting formula $\sigma_{PI}^{0}(E^0/E)^m$, where E^0 is the last tabulated energy beyond the resonances, that is, above all target thresholds, and $-1 \geq m \geq -3$, as described in Nahar & Pradhan (1994); $m = -3$ for the Kramers fit at very high energies.

The DR collision strengths for the narrow and dense resonances in the energy region $\nu_0 < \nu \leq \infty$ below each target excited threshold were obtained using STGFDR. The radiative decay rates for the allowed excited thresholds are given in Table 3.

Level-specific recombination cross sections $\sigma_{\rm RC}(i)$ into various bound levels $i \equiv n(SLJ)$ of the recombined (e + ion) system are obtained from partial photoionization cross sections $\sigma_{\rm PI}(i, g)$ of the level i using the program RECXS. It sums up the level-specific rates and adds with the resonant contributions of high-n ($\nu_0 \leq \nu \leq \infty$) DR for the total recombination rates. As an additional check on the numerical calculations, the total recombination rate coefficients α_R are also calculated from the total recombination collision strength $\Omega_{\rm RC}$, obtained from all the photoionization cross sections, and the DR collision strengths. The difference between the two numerical values is typically a few percent. The background (nonresonant) contribution from the high-n states ($10 < n \leq \infty$) is also included as the "top-up" part (Nahar 1996). This contribution is important at low temperatures where the recombination rate is dominated by RR, but negligible at high temperatures.

4. RESULTS AND DISCUSSION

A self-consistent set of photoionization cross sections, recombination cross sections, and recombination rate coefficients of processes N V + $h\nu \leftrightarrow$ N VI + e, N VI + $h\nu \leftrightarrow$ N VII + e, F VII + $h\nu \leftrightarrow$ F VIII + e, and F VIII + $h\nu \leftrightarrow$ F IX + e are presented and discussed in detail. Results include data for all fine-structure levels up to $n = 10$. The recombination rates are calculated for a wide range of temperatures. Recombination collision strengths ($\Omega_{\rm RC}$) and cross sections ($\sigma_{\rm RC}$) and velocity-weighted recombination rates as functions of photoelectron energies for comparison with laboratory measurements are illustrated. Some important features in photoionization and electron-ion recombination for individual ions are discussed separately below.

4.1. N V, F VII

A total of 99 bound levels for N V and 98 levels for F VIII with $n \leq 10$, $0 \leq l \leq 9$, $0 \leq L \leq 11$, and total angular momentum $1/2 \leq J \leq 17/2$ are obtained (Nahar 2002). The present photoionization and recombination for N V and F VII are self-consistent with the oscillator strengths obtained earlier by Nahar (2002) in the BPRM approximation using the same wave function expansion.

4.1.1. *Photoionization*

The total photoionization cross section ($\sigma_{\rm PI}$) includes ionization into various excited states, whereas the partial cross section refers to ionization into the ground state of the core ion. Both total and partial cross sections are presented for approximately 100 fine-structure

TABLE 4

TOTAL RECOMBINATION RATE COEFFICIENTS $\alpha_R(T)$ FOR N V–VII AND F VII–IX

$\log_{10} T$ (K)	α_R(cm^3 s^{-1})					
	N V	N VI	N VIII	F VII	F VIII	F IX
1.0	9.70E−10	1.50E−09	2.20E−09	1.96E−09	2.73E−09	3.70E−09
1.1	8.53E−10	1.32E−09	1.94E−09	1.73E−09	2.41E−09	3.27E−09
1.2	7.49E−10	1.16E−09	1.71E−09	1.52E−09	2.13E−09	2.89E−09
1.3	6.57E−10	1.02E−09	1.51E−09	1.34E−09	1.88E−09	2.55E−09
1.4	5.77E−10	8.97E−10	1.33E−09	1.18E−09	1.65E−09	2.25E−09
1.5	5.05E−10	7.88E−10	1.17E−09	1.03E−09	1.46E−09	1.99E−09
1.6	4.42E−10	6.91E−10	1.03E−09	9.07E−10	1.28E−09	1.75E−09
1.7	3.87E−10	6.06E−10	9.02E−10	7.95E−10	1.12E−09	1.54E−09
1.8	3.38E−10	5.31E−10	7.94E−10	6.98E−10	9.87E−10	1.35E−09
1.9	2.95E−10	4.65E−10	6.95E−10	6.10E−10	8.65E−10	1.19E−09
2.0	2.57E−10	4.07E−10	6.10E−10	5.33E−10	7.58E−10	1.04E−09
2.1	2.25E−10	3.55E−10	5.34E−10	4.66E−10	6.64E−10	9.17E−10
2.2	1.96E−10	3.10E−10	4.68E−10	4.07E−10	5.80E−10	8.03E−10
2.3	1.70E−10	2.71E−10	4.09E−10	3.55E−10	5.08E−10	7.03E−10
2.4	1.48E−10	2.36E−10	3.58E−10	3.10E−10	4.44E−10	6.16E−10
2.5	1.29E−10	2.06E−10	3.13E−10	2.70E−10	3.87E−10	5.39E−10
2.6	1.12E−10	1.79E−10	2.73E−10	2.35E−10	3.38E−10	4.72E−10
2.7	9.74E−11	1.56E−10	2.38E−10	2.04E−10	2.95E−10	4.12E−10
2.8	8.44E−11	1.36E−10	2.08E−10	1.78E−10	2.57E−10	3.60E−10
2.9	7.32E−11	1.18E−10	1.81E−10	1.54E−10	2.24E−10	3.14E−10
3.0	6.34E−11	1.03E−10	1.58E−10	1.34E−10	1.95E−10	2.74E−10
3.1	5.49E−11	8.93E−11	1.38E−10	1.16E−10	1.70E−10	2.39E−10
3.2	4.75E−11	7.75E−11	1.20E−10	1.01E−10	1.47E−10	2.09E−10
3.3	4.10E−11	6.72E−11	1.04E−10	8.73E−11	1.28E−10	1.82E−10
3.4	3.54E−11	5.83E−11	9.07E−11	7.55E−11	1.11E−10	1.58E−10
3.5	3.06E−11	5.05E−11	7.89E−11	6.53E−11	9.65E−11	1.38E−10
3.6	2.63E−11	4.37E−11	6.85E−11	5.64E−11	8.37E−11	1.20E−10
3.7	2.27E−11	3.78E−11	5.95E−11	4.87E−11	7.25E−11	1.04E−10
3.8	1.95E−11	3.26E−11	5.16E−11	4.20E−11	6.28E−11	9.04E−11
3.9	1.67E−11	2.82E−11	4.46E−11	3.61E−11	5.43E−11	7.84E−11
4.0	1.43E−11	2.43E−11	3.88E−11	3.11E−11	4.69E−11	6.81E−11
4.1	1.23E−11	2.10E−11	3.35E−11	2.67E−11	4.06E−11	5.89E−11
4.2	1.05E−11	1.81E−11	2.90E−11	2.29E−11	3.50E−11	5.12E−11
4.3	8.96E−12	1.55E−11	2.50E−11	1.97E−11	3.02E−11	4.42E−11
4.4	7.64E−12	1.34E−11	2.16E−11	1.68E−11	2.60E−11	3.82E−11
4.5	6.50E−12	1.15E−11	1.86E−11	1.44E−11	2.24E−11	3.31E−11
4.6	5.51E−12	9.85E−12	1.61E−11	1.23E−11	1.92E−11	2.85E−11
4.7	4.68E−12	8.44E−12	1.38E−11	1.05E−11	1.65E−11	2.46E−11
4.8	3.96E−12	7.23E−12	1.19E−11	8.90E−12	1.42E−11	2.12E−11
4.9	3.34E−12	6.19E−12	1.02E−11	7.55E−12	1.22E−11	1.83E−11
5.0	2.81E−12	5.28E−12	8.76E−12	6.41E−12	1.04E−11	1.57E−11
5.1	2.36E−12	4.51E−12	7.49E−12	5.42E−12	8.91E−12	1.35E−11
5.2	1.98E−12	3.84E−12	6.41E−12	4.57E−12	7.60E−12	1.16E−11
5.3	1.65E−12	3.27E−12	5.48E−12	3.85E−12	6.49E−12	9.91E−12
5.4	1.38E−12	2.78E−12	4.67E−12	3.23E−12	5.52E−12	8.48E−12
5.5	1.14E−12	2.36E−12	3.98E−12	2.71E−12	4.70E−12	7.25E−12
5.6	9.47E−13	2.00E−12	3.38E−12	2.26E−12	3.99E−12	6.18E−12
5.7	7.92E−13	1.69E−12	2.87E−12	1.88E−12	3.38E−12	5.27E−12
5.8	6.86E−13	1.44E−12	2.43E−12	1.56E−12	2.86E−12	4.48E−12
5.9	6.57E−13	1.27E−12	2.05E−12	1.30E−12	2.42E−12	3.80E−12
6.0	7.23E−13	1.22E−12	1.73E−12	1.10E−12	2.05E−12	3.22E−12
6.1	8.72E−13	1.29E−12	1.45E−12	1.01E−12	1.77E−12	2.71E−12
6.2	1.06E−12	1.46E−12	1.22E−12	1.05E−12	1.60E−12	2.30E−12
6.3	1.21E−12	1.66E−12	1.02E−12	1.23E−12	1.55E−12	1.93E−12
6.4	1.30E−12	1.81E−12	8.46E−13	1.49E−12	1.60E−12	1.62E−12
6.5	1.29E−12	1.87E−12	7.02E−13	1.75E−12	1.69E−12	1.35E−12
6.6	1.21E−12	1.81E−12	5.80E−13	1.92E−12	1.76E−12	1.13E−12
6.7	1.07E−12	1.66E−12	4.77E−13	1.95E−12	1.76E−12	9.35E−13
6.8	9.11E−13	1.45E−12	3.91E−13	1.87E−12	1.68E−12	7.72E−13
6.9	7.46E−13	1.22E−12	3.17E−13	1.69E−12	1.53E−12	6.36E−13
7.0	5.94E−13	9.92E−13	2.58E−13	1.45E−12	1.33E−12	5.21E−13
7.1	4.63E−13	7.87E−13	2.07E−13	1.20E−12	1.12E−12	4.24E−13

TABLE 4—*Continued*

$\log_{10} T$ (K)	α_R(cm^3 s^{-1})					
	N V	N VI	N VIII	F VII	F VIII	F IX
7.2	3.53E−13	6.12E−13	1.66E−13	9.67E−13	9.13E−13	3.45E−13
7.3	2.66E−13	4.68E−13	1.32E−13	7.58E−13	7.27E−13	2.77E−13
7.4	1.98E−13	3.53E−13	1.04E−13	5.83E−13	5.68E−13	2.22E−13
7.5	1.46E−13	2.64E−13	8.21E−14	4.41E−13	4.37E−13	1.77E−13
7.6	1.07E−13	1.96E−13	6.41E−14	3.29E−13	3.31E−13	1.40E−13
7.7	7.79E−14	1.44E−13	4.98E−14	2.44E−13	2.49E−13	1.10E−13
7.8	5.65E−14	1.06E−13	3.85E−14	1.79E−13	1.86E−13	8.63E−14
7.9	4.08E−14	7.72E−14	2.95E−14	1.30E−13	1.38E−13	6.71E−14
8.0	2.93E−14	5.62E−14	2.26E−14	9.46E−14	1.02E−13	5.20E−14
8.1	2.11E−14	4.08E−14	1.71E−14	6.84E−14	7.48E−14	3.98E−14
8.2	1.51E−14	2.96E−14	1.29E−14	4.93E−14	5.48E−14	3.06E−14
8.3	1.08E−14	2.14E−14	9.73E−15	3.54E−14	4.00E−14	2.32E−14
8.4	7.74E−15	1.54E−14	7.28E−15	2.54E−14	2.92E−14	1.75E−14
8.5	5.53E−15	1.11E−14	5.43E−15	1.82E−14	2.13E−14	1.32E−14
8.6	3.95E−15	8.04E−15	4.03E−15	1.30E−14	1.55E−14	9.88E−15
8.7	2.82E−15	5.79E−15	2.98E−15	9.30E−15	1.12E−14	7.37E−15
8.8	2.01E−15	4.17E−15	2.20E−15	6.64E−15	8.16E−15	5.47E−15
8.9	1.43E−15	3.00E−15	1.61E−15	4.74E−15	5.92E−15	4.05E−15
9.0	1.02E−15	2.16E−15	1.18E−15	3.38E−15	4.29E−15	2.99E−15

bound levels of N V and F VII. Salient features of some of the levels are illustrated below.

Figures 1 and 2 show photoionization cross sections for the ground states ($1s^2 2s^2 S_{1/2}$) of N V and F VII, respectively. The features are very similar for these two Li-like ions. The top panel in each figure presents the total photoionization cross section, which is summed over contributions from channels with various target thresholds for ionization, and the bottom panel presents the *partial* cross section for ionization into the ground $1s^2(^1S_0)$ level of residual ions N VI and F VIII. Since the first excited levels of the $n = 2$ thresholds of the core lie at high energies, the cross section decreases monotonically over a large energy range before the Rydberg series of resonances appear. The resonances belong to the Rydberg series converging onto the $n = 2$ and 3 levels of the core ion. The initial resonance complexes are the well-known KLL, KLM, etc., complexes belonging to $n = 2$ core thresholds as discussed by Nahar et al. (2003). KLL denotes the series $1s2l2l$, KLM denotes $1s2l3l'$, etc. The total and the partial cross sections are identical below the first excited level of the residual ion. However, the total $\sigma_{\rm PI}$ is enhanced by the added contributions from excited channels compared to the partial cross sections. The enhancement at the excited $n = 2$ thresholds in the total cross sections is due to K-shell photoionization:

$$h\nu + (1s^2\ 2s) \longrightarrow e + (1s2s,\ 1s2p).$$

This inner-shell edge plays an important role in X-ray photoionization models.

Figure 3 presents total photoionization cross sections of the excited Rydberg series of levels $1s^2 np(^2P^o_{1/2})$, $2 \le n \le 7$, of N V illustrating the resonant structures at higher energies, especially the photoexcitation-of-core (PEC) resonances. The PEC resonances are associated with dipole transitions in the core ion and show up at these excited threshold energies, as shown in the figure by arrows. They are at photon energies of about 31.65 and 36.51 ryd of thresholds $1s2p\ ^3P^o_1,\ ^1P^o_1$ of the $n = 2$ and $1s3p\ ^3P^o_1,\ ^1P^o_1$ of the $n = 3$ levels. The core goes through the allowed $\Delta J = 0$–1 transitions at these photon energies, while

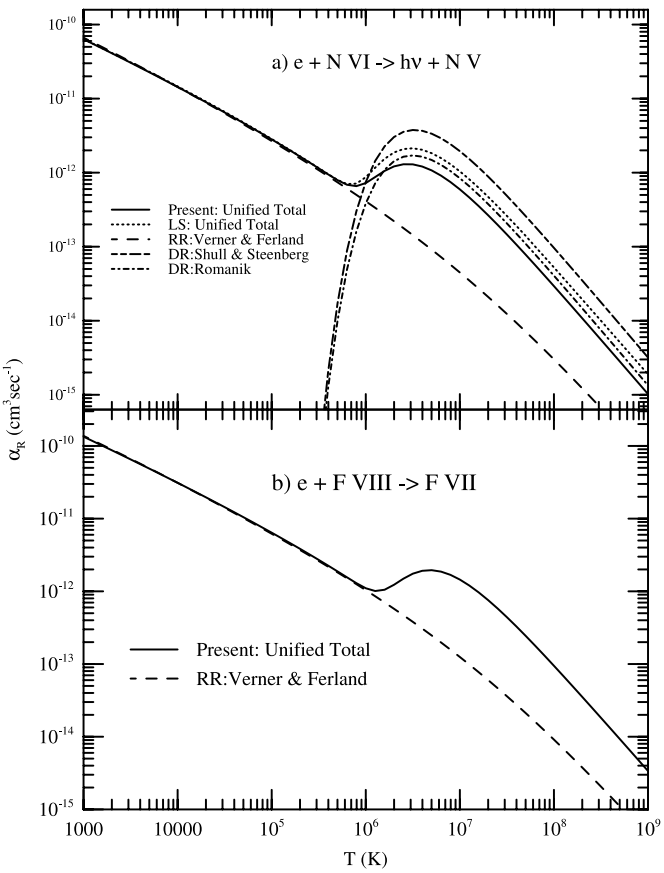

FIG. 6.—Total unified recombination rate coefficients $\alpha_R(T)$ (*solid curves*) for (*a*) N V and (*b*) F VII. The RR rates are from Verner & Ferland (1996; *dashed curves*). For N V, the total unified rate in *LS* coupling is from Nahar & Pradhan (1997; *dotted curve*), and the DR rates are from Shull & Steenberg (1982; *short-dashed–long-dashed curve*) and Romanik (1988; *dot-dashed curve*).

TABLE 5

LEVEL-SPECIFIC RECOMBINATION RATE COEFFICIENTS FOR THE GROUND AND EXCITED $2l$ AND $3l$ LEVELS OF N V AND F VII

$\log_{10} T$ (K)	α_R(cm^3 s^{-1})							
	$2s\ ^2S_{1/2}$	$3s\ ^2S_{1/2}$	$2p\ ^2P^o_{1/2}$	$3p\ ^2P^o_{1/2}$	$3d\ ^2D_{3/2}$	$2p\ ^2P^o_{3/2}$	$3p\ ^2P^o_{3/2}$	$3d\ ^2D_{5/2}$
	N V							
	BE = −7.19	−3.04	−6.46	−2.84	−2.78	−6.46	−2.84	−2.78
1.0	1.93E−11	5.70E−12	2.03E−11	7.37E−12	9.40E−12	4.05E−11	1.47E−11	1.41E−11
1.1	1.72E−11	5.08E−12	1.81E−11	6.57E−12	8.38E−12	3.61E−11	1.31E−11	1.26E−11
1.2	1.53E−11	4.53E−12	1.61E−11	5.85E−12	7.47E−12	3.22E−11	1.17E−11	1.12E−11
1.3	1.37E−11	4.04E−12	1.44E−11	5.22E−12	6.66E−12	2.87E−11	1.04E−11	9.98E−12
1.4	1.22E−11	3.60E−12	1.28E−11	4.65E−12	5.93E−12	2.56E−11	9.29E−12	8.89E−12
1.5	1.09E−11	3.21E−12	1.14E−11	4.14E−12	5.29E−12	2.28E−11	8.28E−12	7.93E−12
1.6	9.68E−12	2.86E−12	1.02E−11	3.69E−12	4.71E−12	2.03E−11	7.38E−12	7.07E−12
1.7	8.63E−12	2.55E−12	9.07E−12	3.29E−12	4.20E−12	1.81E−11	6.58E−12	6.30E−12
1.8	7.69E−12	2.27E−12	8.08E−12	2.93E−12	3.74E−12	1.61E−11	5.86E−12	5.61E−12
1.9	6.86E−12	2.02E−12	7.20E−12	2.61E−12	3.34E−12	1.44E−11	5.22E−12	5.00E−12
2.0	6.11E−12	1.80E−12	6.42E−12	2.33E−12	2.97E−12	1.28E−11	4.66E−12	4.46E−12
2.1	5.45E−12	1.61E−12	5.72E−12	2.08E−12	2.65E−12	1.14E−11	4.15E−12	3.97E−12
2.2	4.85E−12	1.43E−12	5.10E−12	1.85E−12	2.36E−12	1.02E−11	3.70E−12	3.54E−12
2.3	4.33E−12	1.28E−12	4.54E−12	1.65E−12	2.10E−12	9.07E−12	3.30E−12	3.15E−12
2.4	3.86E−12	1.14E−12	4.05E−12	1.47E−12	1.87E−12	8.09E−12	2.94E−12	2.81E−12
2.5	3.44E−12	1.01E−12	3.61E−12	1.31E−12	1.67E−12	7.21E−12	2.62E−12	2.50E−12
2.6	3.06E−12	9.04E−13	3.22E−12	1.17E−12	1.49E−12	6.42E−12	2.33E−12	2.23E−12
2.7	2.73E−12	8.06E−13	2.87E−12	1.04E−12	1.33E−12	5.72E−12	2.08E−12	1.99E−12
2.8	2.43E−12	7.18E−13	2.55E−12	9.27E−13	1.18E−12	5.10E−12	1.85E−12	1.77E−12
2.9	2.17E−12	6.40E−13	2.28E−12	8.26E−13	1.05E−12	4.55E−12	1.65E−12	1.58E−12
3.0	1.93E−12	5.71E−13	2.03E−12	7.36E−13	9.37E−13	4.05E−12	1.47E−12	1.41E−12
3.1	1.72E−12	5.09E−13	1.81E−12	6.56E−13	8.35E−13	3.61E−12	1.31E−12	1.25E−12
3.2	1.54E−12	4.53E−13	1.61E−12	5.85E−13	7.43E−13	3.22E−12	1.17E−12	1.11E−12
3.3	1.37E−12	4.04E−13	1.43E−12	5.21E−13	6.62E−13	2.86E−12	1.04E−12	9.92E−13
3.4	1.22E−12	3.60E−13	1.28E−12	4.64E−13	5.89E−13	2.55E−12	9.27E−13	8.82E−13
3.5	1.09E−12	3.21E−13	1.14E−12	4.13E−13	5.24E−13	2.27E−12	8.26E−13	7.85E−13
3.6	9.69E−13	2.86E−13	1.01E−12	3.68E−13	4.65E−13	2.02E−12	7.36E−13	6.98E−13
3.7	8.64E−13	2.55E−13	9.03E−13	3.28E−13	4.13E−13	1.80E−12	6.55E−13	6.20E−13
3.8	7.70E−13	2.28E−13	8.04E−13	2.92E−13	3.67E−13	1.60E−12	5.84E−13	5.50E−13
3.9	6.87E−13	2.03E−13	7.15E−13	2.60E−13	3.25E−13	1.43E−12	5.19E−13	4.88E−13
4.0	6.12E−13	1.81E−13	6.36E−13	2.31E−13	2.88E−13	1.27E−12	4.62E−13	4.32E−13
4.1	5.46E−13	1.62E−13	5.66E−13	2.06E−13	2.55E−13	1.13E−12	4.11E−13	3.82E−13
4.2	4.87E−13	1.44E−13	5.03E−13	1.83E−13	2.25E−13	1.00E−12	3.66E−13	3.37E−13
4.3	4.34E−13	1.29E−13	4.46E−13	1.63E−13	1.98E−13	8.91E−13	3.25E−13	2.97E−13
4.4	3.87E−13	1.15E−13	3.96E−13	1.44E−13	1.74E−13	7.91E−13	2.88E−13	2.61E−13
4.5	3.46E−13	1.03E−13	3.51E−13	1.28E−13	1.52E−13	7.01E−13	2.56E−13	2.28E−13
4.6	3.09E−13	9.19E−14	3.11E−13	1.13E−13	1.33E−13	6.20E−13	2.26E−13	1.99E−13
4.7	2.76E−13	8.22E−14	2.74E−13	1.00E−13	1.15E−13	5.48E−13	2.00E−13	1.73E−13
4.8	2.46E−13	7.35E−14	2.42E−13	8.84E−14	9.94E−14	4.83E−13	1.77E−13	1.49E−13
4.9	2.20E−13	6.58E−14	2.13E−13	7.78E−14	8.53E−14	4.25E−13	1.56E−13	1.28E−13
5.0	1.97E−13	5.89E−14	1.87E−13	6.83E−14	7.26E−14	3.73E−13	1.37E−13	1.09E−13
5.1	1.76E−13	5.28E−14	1.63E−13	5.98E−14	6.14E−14	3.26E−13	1.19E−13	9.21E−14
5.2	1.57E−13	4.73E−14	1.42E−13	5.21E−14	5.15E−14	2.84E−13	1.04E−13	7.72E−14
5.3	1.41E−13	4.24E−14	1.23E−13	4.52E−14	4.28E−14	2.46E−13	9.02E−14	6.42E−14
5.4	1.26E−13	3.80E−14	1.06E−13	3.90E−14	3.52E−14	2.12E−13	7.78E−14	5.28E−14
5.5	1.13E−13	3.40E−14	9.10E−14	3.34E−14	2.87E−14	1.82E−13	6.67E−14	4.30E−14
5.6	1.02E−13	3.05E−14	7.76E−14	2.85E−14	2.33E−14	1.55E−13	5.69E−14	3.48E−14
5.7	9.30E−14	2.76E−14	6.64E−14	2.44E−14	1.96E−14	1.33E−13	4.87E−14	2.80E−14
5.8	9.00E−14	2.62E−14	5.84E−14	2.19E−14	1.95E−14	1.17E−13	4.35E−14	2.34E−14
5.9	9.59E−14	2.77E−14	5.48E−14	2.21E−14	2.67E−14	1.09E−13	4.35E−14	2.19E−14
6.0	1.11E−13	3.30E−14	5.61E−14	2.61E−14	4.38E−14	1.12E−13	5.06E−14	2.44E−14
6.1	1.33E−13	4.17E−14	6.11E−14	3.33E−14	6.99E−14	1.23E−13	6.39E−14	3.03E−14
6.2	1.54E−13	5.14E−14	6.68E−14	4.17E−14	9.90E−14	1.35E−13	7.95E−14	3.77E−14
6.3	1.69E−13	5.93E−14	7.07E−14	4.88E−14	1.24E−13	1.43E−13	9.27E−14	4.42E−14
6.4	1.72E−13	6.33E−14	7.09E−14	5.27E−14	1.38E−13	1.43E−13	9.98E−14	4.78E−14
6.5	1.65E−13	6.29E−14	6.72E−14	5.26E−14	1.41E−13	1.36E−13	9.96E−14	4.79E−14
6.6	1.50E−13	5.86E−14	6.06E−14	4.92E−14	1.34E−13	1.23E−13	9.31E−14	4.49E−14
6.7	1.30E−13	5.19E−14	5.23E−14	4.36E−14	1.20E−13	1.06E−13	8.25E−14	3.99E−14
6.8	1.09E−13	4.40E−14	4.34E−14	3.70E−14	1.02E−13	8.83E−14	6.99E−14	3.38E−14
6.9	8.86E−14	3.61E−14	3.50E−14	3.02E−14	8.36E−14	7.12E−14	5.71E−14	2.77E−14
7.0	7.02E−14	2.88E−14	2.75E−14	2.40E−14	6.65E−14	5.61E−14	4.54E−14	2.20E−14

TABLE 5—*Continued*

$\log_{10} T$ (K)	α_R(cm^3 s^{-1})							
	$2s\ ^2S_{1/2}$	$3s\ ^2S_{1/2}$	$2p\ ^2P^o_{1/2}$	$3p\ ^2P^o_{1/2}$	$3d\ ^2D_{3/2}$	$2p\ ^2P^o_{3/2}$	$3p\ ^2P^o_{3/2}$	$3d\ ^2D_{5/2}$
	N V							
	BE = −7.19	−3.04	−6.46	−2.84	−2.78	−6.46	−2.84	−2.78
7.1	5.46E−14	2.24E−14	2.12E−14	1.86E−14	5.17E−14	4.32E−14	3.52E−14	1.71E−14
7.2	4.18E−14	1.72E−14	1.61E−14	1.42E−14	3.94E−14	3.28E−14	2.69E−14	1.30E−14
7.3	3.16E−14	1.30E−14	1.21E−14	1.07E−14	2.96E−14	2.46E−14	2.02E−14	9.76E−15
7.4	2.37E−14	9.71E−15	8.96E−15	7.92E−15	2.19E−14	1.83E−14	1.50E−14	7.24E−15
7.5	1.76E−14	7.20E−15	6.59E−15	5.83E−15	1.61E−14	1.34E−14	1.10E−14	5.32E−15
7.6	1.30E−14	5.30E−15	4.82E−15	4.26E−15	1.18E−14	9.83E−15	8.05E−15	3.88E−15
7.7	9.55E−15	3.88E−15	3.51E−15	3.09E−15	8.52E−15	7.15E−15	5.85E−15	2.81E−15
7.8	7.00E−15	2.83E−15	2.54E−15	2.23E−15	6.14E−15	5.18E−15	4.23E−15	2.03E−15
7.9	5.11E−15	2.05E−15	1.84E−15	1.61E−15	4.41E−15	3.74E−15	3.04E−15	1.46E−15
8.0	3.72E−15	1.49E−15	1.32E−15	1.15E−15	3.16E−15	2.70E−15	2.19E−15	1.04E−15
8.1	2.70E−15	1.07E−15	9.52E−16	8.27E−16	2.26E−15	1.94E−15	1.57E−15	7.46E−16
8.2	1.96E−15	7.75E−16	6.84E−16	5.91E−16	1.61E−15	1.39E−15	1.12E−15	5.32E−16
8.3	1.42E−15	5.58E−16	4.90E−16	4.22E−16	1.15E−15	9.98E−16	7.99E−16	3.79E−16
8.4	1.03E−15	4.02E−16	3.51E−16	3.01E−16	8.17E−16	7.15E−16	5.70E−16	2.70E−16
8.5	7.45E−16	2.89E−16	2.52E−16	2.15E−16	5.80E−16	5.12E−16	4.06E−16	1.92E−16
8.6	5.38E−16	2.07E−16	1.80E−16	1.53E−16	4.12E−16	3.66E−16	2.89E−16	1.36E−16
8.7	3.89E−16	1.49E−16	1.29E−16	1.09E−16	2.92E−16	2.62E−16	2.06E−16	9.66E−17
8.8	2.81E−16	1.07E−16	9.19E−17	7.73E−17	2.07E−16	1.87E−16	1.47E−16	6.86E−17
8.9	2.02E−16	7.67E−17	6.57E−17	5.50E−17	1.47E−16	1.34E−16	1.04E−16	4.86E−17
9.0	1.46E−16	5.50E−17	4.69E−17	3.91E−17	1.04E−16	9.54E−17	7.41E−17	3.45E−17
	F VII							
	BE = −13.6	−5.82	−12.6	−5.55	−5.45	−12.6	−5.54	−5.45
1.0	3.83E−11	1.12E−11	3.86E−11	1.35E−11	1.79E−11	7.71E−11	2.70E−11	2.68E−11
1.1	3.41E−11	1.00E−11	3.44E−11	1.20E−11	1.60E−11	6.87E−11	2.41E−11	2.39E−11
1.2	3.04E−11	8.91E−12	3.07E−11	1.07E−11	1.42E−11	6.12E−11	2.14E−11	2.13E−11
1.3	2.71E−11	7.94E−12	2.73E−11	9.57E−12	1.27E−11	5.46E−11	1.91E−11	1.90E−11
1.4	2.42E−11	7.08E−12	2.44E−11	8.53E−12	1.13E−11	4.86E−11	1.70E−11	1.69E−11
1.5	2.15E−11	6.31E−12	2.17E−11	7.60E−12	1.01E−11	4.33E−11	1.52E−11	1.51E−11
1.6	1.92E−11	5.62E−12	1.94E−11	6.77E−12	8.98E−12	3.86E−11	1.35E−11	1.34E−11
1.7	1.71E−11	5.01E−12	1.73E−11	6.04E−12	8.00E−12	3.44E−11	1.21E−11	1.20E−11
1.8	1.53E−11	4.47E−12	1.54E−11	5.38E−12	7.13E−12	3.07E−11	1.07E−11	1.07E−11
1.9	1.36E−11	3.98E−12	1.37E−11	4.80E−12	6.35E−12	2.73E−11	9.58E−12	9.52E−12
2.0	1.21E−11	3.55E−12	1.22E−11	4.27E−12	5.66E−12	2.44E−11	8.54E−12	8.48E−12
2.1	1.08E−11	3.16E−12	1.09E−11	3.81E−12	5.05E−12	2.17E−11	7.61E−12	7.56E−12
2.2	9.62E−12	2.82E−12	9.70E−12	3.40E−12	4.50E−12	1.94E−11	6.78E−12	6.74E−12
2.3	8.58E−12	2.51E−12	8.65E−12	3.03E−12	4.01E−12	1.72E−11	6.05E−12	6.01E−12
2.4	7.64E−12	2.24E−12	7.71E−12	2.70E−12	3.57E−12	1.54E−11	5.39E−12	5.35E−12
2.5	6.81E−12	2.00E−12	6.87E−12	2.40E−12	3.18E−12	1.37E−11	4.80E−12	4.77E−12
2.6	6.07E−12	1.78E−12	6.12E−12	2.14E−12	2.84E−12	1.22E−11	4.28E−12	4.25E−12
2.7	5.41E−12	1.59E−12	5.46E−12	1.91E−12	2.53E−12	1.09E−11	3.81E−12	3.79E−12
2.8	4.82E−12	1.41E−12	4.86E−12	1.70E−12	2.25E−12	9.70E−12	3.40E−12	3.38E−12
2.9	4.30E−12	1.26E−12	4.33E−12	1.52E−12	2.01E−12	8.64E−12	3.03E−12	3.01E−12
3.0	3.83E−12	1.12E−12	3.86E−12	1.35E−12	1.79E−12	7.70E−12	2.70E−12	2.68E−12
3.1	3.42E−12	1.00E−12	3.44E−12	1.20E−12	1.59E−12	6.86E−12	2.41E−12	2.39E−12
3.2	3.04E−12	8.91E−13	3.07E−12	1.07E−12	1.42E−12	6.12E−12	2.14E−12	2.13E−12
3.3	2.71E−12	7.95E−13	2.73E−12	9.56E−13	1.26E−12	5.45E−12	1.91E−12	1.89E−12
3.4	2.42E−12	7.08E−13	2.43E−12	8.52E−13	1.13E−12	4.86E−12	1.70E−12	1.69E−12
3.5	2.15E−12	6.31E−13	2.17E−12	7.59E−13	1.00E−12	4.33E−12	1.52E−12	1.50E−12
3.6	1.92E−12	5.63E−13	1.93E−12	6.76E−13	8.92E−13	3.85E−12	1.35E−12	1.34E−12
3.7	1.71E−12	5.01E−13	1.72E−12	6.03E−13	7.94E−13	3.43E−12	1.20E−12	1.19E−12
3.8	1.53E−12	4.47E−13	1.53E−12	5.37E−13	7.06E−13	3.06E−12	1.07E−12	1.06E−12
3.9	1.36E−12	3.98E−13	1.37E−12	4.78E−13	6.28E−13	2.72E−12	9.55E−13	9.41E−13
4.0	1.21E−12	3.55E−13	1.22E−12	4.26E−13	5.58E−13	2.42E−12	8.51E−13	8.36E−13
4.1	1.08E−12	3.17E−13	1.08E−12	3.79E−13	4.96E−13	2.16E−12	7.57E−13	7.43E−13
4.2	9.64E−13	2.82E−13	9.63E−13	3.38E−13	4.40E−13	1.92E−12	6.74E−13	6.59E−13
4.3	8.59E−13	2.52E−13	8.57E−13	3.00E−13	3.90E−13	1.71E−12	6.00E−13	5.84E−13
4.4	7.66E−13	2.25E−13	7.62E−13	2.67E−13	3.45E−13	1.52E−12	5.34E−13	5.17E−13
4.5	6.83E−13	2.00E−13	6.77E−13	2.38E−13	3.05E−13	1.35E−12	4.75E−13	4.57E−13
4.6	6.09E−13	1.79E−13	6.01E−13	2.11E−13	2.69E−13	1.20E−12	4.22E−13	4.03E−13
4.7	5.44E−13	1.60E−13	5.33E−13	1.88E−13	2.36E−13	1.06E−12	3.76E−13	3.54E−13

TABLE 5—*Continued*

$\log_{10} T$ (K)	α_R(cm^3 s^{-1})							
	$2s\ ^2S_{1/2}$	$3s\ ^2S_{1/2}$	$2p\ ^2P^o_{1/2}$	$3p\ ^2P^o_{1/2}$	$3d\ ^2D_{3/2}$	$2p\ ^2P^o_{3/2}$	$3p\ ^2P^o_{3/2}$	$3d\ ^2D_{5/2}$
	F VII							
	BE = −13.6	−5.82	−12.6	−5.55	−5.45	−12.6	−5.54	−5.45
4.8	4.85E−13	1.43E−13	4.72E−13	1.67E−13	2.07E−13	9.42E−13	3.34E−13	3.11E−13
4.9	4.33E−13	1.28E−13	4.18E−13	1.48E−13	1.81E−13	8.33E−13	2.96E−13	2.72E−13
5.0	3.86E−13	1.15E−13	3.69E−13	1.32E−13	1.58E−13	7.36E−13	2.63E−13	2.36E−13
5.1	3.45E−13	1.03E−13	3.25E−13	1.17E−13	1.37E−13	6.48E−13	2.33E−13	2.05E−13
5.2	3.08E−13	9.26E−14	2.86E−13	1.03E−13	1.17E−13	5.70E−13	2.06E−13	1.76E−13
5.3	2.75E−13	8.33E−14	2.51E−13	9.10E−14	1.00E−13	5.00E−13	1.82E−13	1.50E−13
5.4	2.45E−13	7.48E−14	2.19E−13	7.99E−14	8.49E−14	4.36E−13	1.59E−13	1.27E−13
5.5	2.19E−13	6.72E−14	1.90E−13	6.98E−14	7.12E−14	3.79E−13	1.39E−13	1.07E−13
5.6	1.96E−13	6.02E−14	1.65E−13	6.06E−14	5.91E−14	3.28E−13	1.21E−13	8.86E−14
5.7	1.75E−13	5.39E−14	1.42E−13	5.22E−14	4.86E−14	2.83E−13	1.04E−13	7.28E−14
5.8	1.56E−13	4.81E−14	1.22E−13	4.48E−14	3.96E−14	2.42E−13	8.94E−14	5.93E−14
5.9	1.41E−13	4.30E−14	1.04E−13	3.83E−14	3.20E−14	2.08E−13	7.66E−14	4.83E−14
6.0	1.32E−13	3.89E−14	9.09E−14	3.35E−14	2.60E−14	1.81E−13	6.77E−14	4.10E−14
6.1	1.32E−13	3.65E−14	8.36E−14	3.17E−14	2.22E−14	1.67E−13	6.60E−14	4.01E−14
6.2	1.42E−13	3.66E−14	8.31E−14	3.43E−14	2.10E−14	1.68E−13	7.52E−14	4.86E−14
6.3	1.59E−13	3.91E−14	8.82E−14	4.13E−14	2.24E−14	1.80E−13	9.54E−14	6.65E−14
6.4	1.77E−13	4.29E−14	9.52E−14	5.07E−14	2.53E−14	1.96E−13	1.22E−13	8.97E−14
6.5	1.88E−13	4.63E−14	1.00E−13	5.94E−14	2.84E−14	2.09E−13	1.46E−13	1.12E−13
6.6	1.90E−13	4.79E−14	1.01E−13	6.48E−14	3.02E−14	2.12E−13	1.61E−13	1.26E−13
6.7	1.81E−13	4.69E−14	9.60E−14	6.56E−14	3.02E−14	2.04E−13	1.64E−13	1.31E−13
6.8	1.65E−13	4.37E−14	8.70E−14	6.22E−14	2.84E−14	1.86E−13	1.57E−13	1.26E−13
6.9	1.43E−13	3.88E−14	7.54E−14	5.58E−14	2.54E−14	1.62E−13	1.41E−13	1.14E−13
7.0	1.20E−13	3.31E−14	6.30E−14	4.77E−14	2.16E−14	1.36E−13	1.21E−13	9.80E−14
7.1	9.78E−14	2.74E−14	5.10E−14	3.93E−14	1.78E−14	1.10E−13	9.97E−14	8.11E−14
7.2	7.79E−14	2.20E−14	4.03E−14	3.14E−14	1.42E−14	8.72E−14	7.98E−14	6.50E−14
7.3	6.08E−14	1.74E−14	3.12E−14	2.45E−14	1.11E−14	6.76E−14	6.23E−14	5.08E−14
7.4	4.68E−14	1.35E−14	2.37E−14	1.88E−14	8.45E−15	5.15E−14	4.77E−14	3.89E−14
7.5	3.56E−14	1.03E−14	1.78E−14	1.42E−14	6.36E−15	3.87E−14	3.59E−14	2.93E−14
7.6	2.68E−14	7.79E−15	1.33E−14	1.05E−14	4.72E−15	2.88E−14	2.68E−14	2.18E−14
7.7	2.00E−14	5.84E−15	9.79E−15	7.77E−15	3.48E−15	2.13E−14	1.97E−14	1.61E−14
7.8	1.49E−14	4.35E−15	7.18E−15	5.69E−15	2.54E−15	1.56E−14	1.44E−14	1.17E−14
7.9	1.10E−14	3.22E−15	5.23E−15	4.13E−15	1.84E−15	1.14E−14	1.05E−14	8.52E−15
8.0	8.12E−15	2.37E−15	3.80E−15	2.99E−15	1.33E−15	8.24E−15	7.58E−15	6.15E−15
8.1	5.96E−15	1.74E−15	2.75E−15	2.16E−15	9.55E−16	5.97E−15	5.46E−15	4.43E−15
8.2	4.37E−15	1.28E−15	1.99E−15	1.55E−15	6.85E−16	4.30E−15	3.92E−15	3.17E−15
8.3	3.19E−15	9.35E−16	1.43E−15	1.11E−15	4.90E−16	3.10E−15	2.81E−15	2.27E−15
8.4	2.33E−15	6.82E−16	1.03E−15	7.94E−16	3.49E−16	2.23E−15	2.01E−15	1.62E−15
8.5	1.70E−15	4.97E−16	7.39E−16	5.67E−16	2.49E−16	1.60E−15	1.43E−15	1.15E−15
8.6	1.24E−15	3.61E−16	5.31E−16	4.05E−16	1.77E−16	1.15E−15	1.02E−15	8.21E−16
8.7	8.99E−16	2.62E−16	3.80E−16	2.88E−16	1.26E−16	8.22E−16	7.29E−16	5.83E−16
8.8	6.53E−16	1.90E−16	2.73E−16	2.05E−16	8.94E−17	5.89E−16	5.19E−16	4.14E−16
8.9	4.74E−16	1.38E−16	1.95E−16	1.46E−16	6.35E−17	4.21E−16	3.69E−16	2.94E−16
9.0	3.43E−16	1.00E−16	1.40E−16	1.04E−16	4.50E−17	3.01E−16	2.62E−16	2.09E−16

NOTE.—BE is the binding energy of the level in rydbergs.

the outer electron remains a "spectator" in a doubly excited resonant state, which is followed by autoionization into the ground level of the core. PEC resonances are much more enhanced than the typical narrow Rydberg resonances and can increase the background cross sections by orders of magnitude. The PEC effect becomes increasingly prominent for cross sections of higher excited levels and exhibits the non-hydrogenic behavior of the cross sections. PEC resonances exist in photoionization cross sections for *all* excited bound levels of N V and F VII.

4.1.2. *Electron-Ion Recombination*

As explained in § 2, the total recombination cross sections or the collision strengths correspond to summed contributions of photoionization cross sections of all levels. The features of total recombination collision strength ($\Omega_{\rm RC}$) and recombination cross sections ($\sigma_{\rm RC}$) are similar as they are related through kinematic factors (eq. [8]). The unified total $\sigma_{\rm RC}$ for N V and F VII are presented in the top panels of Figures 4 and 5, respectively. The cross section $\sigma_{\rm RC}$ diverges at zero photoelectron energy (eq. [8]). It decays smoothly with energy until the emergence of resonance complexes at high energies. A few resonance complexes are marked in the figures: KLL, KLM, KLN, etc., converging onto the $n = 2$ thresholds, and KMM, KMN, etc., converging onto the $n = 3$ thresholds. These resonances manifest themselves as dielectronic satellite lines observed in tokamaks, electron beam ion traps, ion storage rings, and high-temperature astrophysical

sources. The prominent KLL complex has been well studied in previous works (e.g., Gabriel 1972; Pradhan & Zhang 1997; Oelgoetz & Pradhan 2001) for various ions.

The strong KLL resonances of a Li-like ion are seen as dielectronic satellites, especially for ions more highly charged than the present ions N v and F vii. The profiles and intensities from the unified cross sections can be directly compared with measured quantities and observed recombination spectra (Nahar & Pradhan 2006). The unified cross sections include both the RR and DR contributions. Although DR dominates the satellite lines, a partial RR contribution is inherent in the natural lines. Hence the unified (electron+ion) recombination yields an essentially exact representation of dielectronic satellite spectra.

We calculate the velocity or energy-dependent photorecombination rates,

$$\alpha_{\rm RC}(E) = v\sigma_{\rm RC}(E), \tag{9}$$

where v is the velocity and E is the photoelectron energy, for comparison with experiments. The bottom panels of Figures 4 and 5 present $\alpha_{\rm RC}(E)$ for N vi and F vii, respectively, especially the resonant part of $\alpha_{\rm RC}(E)$ converging onto the $n = 2$ threshold of the respective cores. The measurable feature is this resonant part convolved with the monochromatic bandwidth in the experiment (e.g., as described for C iii in Pradhan et al. [2001]).

The total recombination rate coefficient $\alpha_{\rm RC}(T)$ for N v and F vii is given for a wide range of temperatures. The values are tabulated in Table 4 and the main features are illustrated and compared with the available data for RR and DR rates in Figures 6*a* and 6*b*. These three-electron atomic systems show the basic features in the total recombination rate coefficient (*solid curves*) of starting high at very low temperatures, going down until it rises to form a DR "bump" at high temperatures, and then decaying monotonically. At low temperatures the recombination is via radiative recombination into an infinite number of high-n levels, and at high temperatures the rise is due to the appearance of resonances and the consequent dominance of DR.

The low-T unified recombination rate coefficients for N v and F vii agree very well with the RR rate coefficients by Verner & Ferland (1996; *dashed curves*). However, at high T where DR contributes dominantly, the present recombination rate of N v is lower than that of the earlier unified rates in *LS* coupling (Nahar & Pradhan 1997; *dotted curve*), as well as of other rates. It agrees better with that of Romanik (1988; *dot-dashed curve*), which is between the unified *LS* coupling and BPRM rates. The maximum difference is at the DR peak, where the present rate is lower by 24%. A much larger difference exists with the fit of Shull & Steenberg (1982; *short-dashed–long-dashed curve*).[2] The main reason for the difference is the inclusion of radiation damping of autoionizing resonances, which reduces the resonance peaks and thus lowers the rates. Radiation damping is significant for these ions as the radiative decay rate is comparable to that of autoionization. The effect was not considered in the unified *LS* coupling calculations. The relativistic fine-structure splitting enabled finer resolution of resonances and hence higher accuracy for the photoionization cross sections and for the recombination rates. There is no DR rate available for F vii for comparison.

Level-specific recombination rate coefficients $\alpha_R(T, i)$ of N v and F vii are presented for about 100 levels. They correspond to all associated $J\pi$ levels $i \equiv n(SLJ)$ with $n \leq 10$ and $l \leq 9$. Table 5 presents $\alpha_R(T, i)$ into the eight lowest excited $n = 2$ and 3 levels of $n(SLJ)$, $1s^2 2s\,^2S_0$, $1s^2 2p\ ^2P^o_{1/2,\,3/2}$, $1s^2 3s\,^2S_0$, $1s^2 3p\ ^2P^o_{1/2,\,3/2}$, and $1s^2 3d\ ^2D_{3/2,\,5/2}$, which are often needed for spectral modeling in the UV region. These rates show smooth features with a DR "shoulder."

[2] The values are fitted from the works of V. L. Jacobs and coworkers as referenced in Shull & van Steenberg (1982).

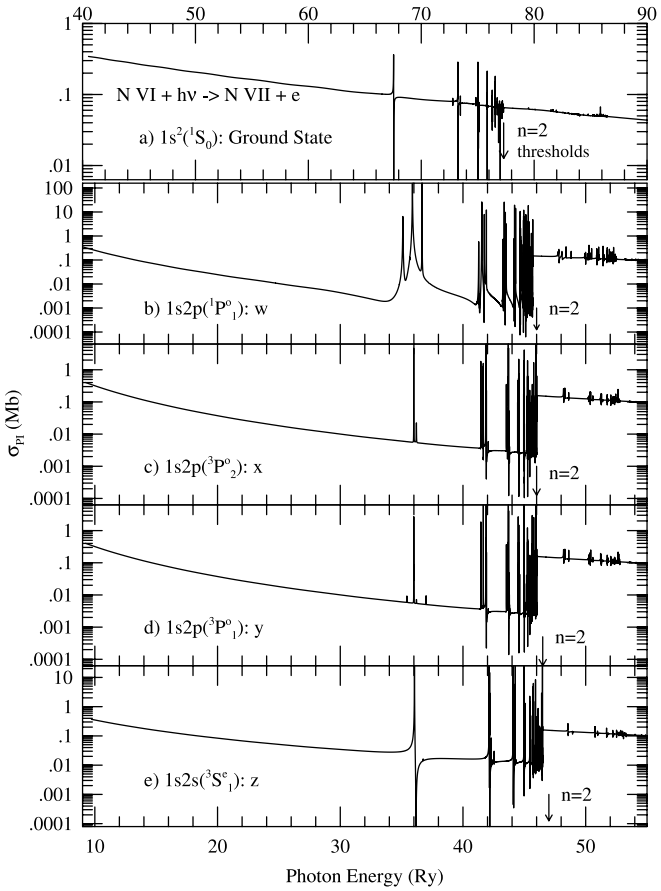

FIG. 7.—Level-specific photoionization cross sections of N vi. (*a*) The ground level, $1s^2$ ($^1S_0$), and four excited (*b*) $1s2p(^1P^o_1)$, (*c*) $1s2p(^3P^o_2)$, (*d*) $1s2p(^3P^o_1)$, and (*e*) $1s2s(^3S_1)$ levels corresponding to the prominent resonance (*w*), intercombination (*y*), and forbidden (*x*, *z*) diagnostic X-ray lines. The K-shell ionization edge is noticed at the $n = 2$ thresholds for the excited levels.

4.2. N vi *and* F viii

The total number of fine-structure levels with $n \leq 10$, $0 \leq l \leq 9$, $0 \leq L \leq 14$, and total angular momentum $0 \leq J \leq 10$ obtained for N vi is 172 and for F viii is 178. The following two subsections describe the important features for photoionization and recombination for these ions.

4.2.1. *Photoionization*

Partial and total cross sections for N vi and F viii are presented for all bound levels with $n \leq 10$. Illustrative features for these He-like ions are shown in Figure 7 for N vi and Figure 8 for F viii. They present level-specific total photoionization cross sections of the ground level, $1s^2$ ($^1S_0$) (panel *a*), and the four lowest $n = 2$ excited levels (panels *b*–*e*). These excited levels correspond to prominent X-ray lines of the Kα complex of He-like ions: the resonance line [*w*: $1s^2$ ($^1S_0$) $\leftarrow$ $1s2p(^1P^o_1)$], the intercombination line [*y*: $1s^2$ ($^1S_0$) $\leftarrow$ $1s2p(^3P^o_1)$], and the forbidden lines (*x*: $1s^2$ ($^1S_0$) $\leftarrow$ $1s2p(^3P^o_2)$; and *z*: $1s^2$ ($^1S_0$) $\leftarrow$ $1s2s(^3S_1)$], respectively. They are most commonly used in spectral diagnostics of temperature, density, ionization balance, and abundances in plasma sources.

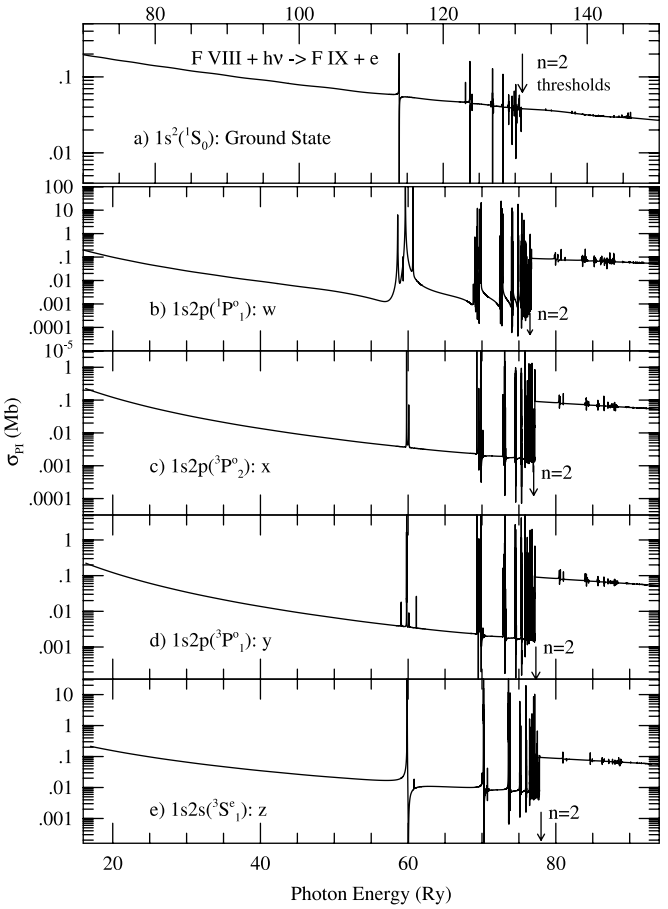

FIG. 8.—Level-specific photoionization cross sections of F VIII. (*a*) The ground level, $1s^2\ (^1S_0)$, and four excited (*b*) $1s2p(^1P^o_1)$, (*c*) $1s2p(^3P^o_2)$, (*d*) $1s2p(^3P^o_1)$, and (*e*) $1s2s(^3S_1)$ levels corresponding to the prominent resonance (*w*), intercombination (*y*), and forbidden (*x*, *z*) diagnostic X-ray lines. The K-shell ionization edge is noticed at the $n = 2$ thresholds for the excited levels.

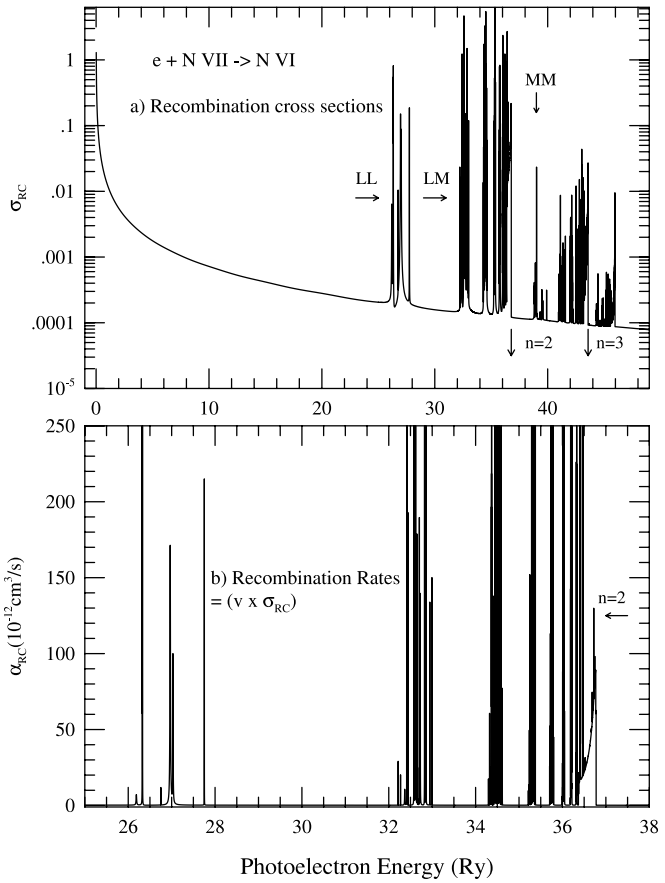

FIG. 9.—(*a*) Total unified (e + ion) recombination cross sections, σ_{RC}, and (*b*) unified recombination rate coefficients, $\alpha_{RC}(E)$, vs. photoelectron energy for (e + N VII → N VI). Note the separated resonance complexes LL, LM, etc., of the $n = 2$; MM, MN, etc., of the $n = 3$; and NN, etc., of the $n = 4$ thresholds. The coefficient $\alpha_{RC}(E)$, convolved with an energy bandwidth, is a measurable quantity.

The cross sections for both N VI and F VIII can be seen to decrease monotonically over a large energy range for all levels. As the excited core levels of these ions lie high in energy, the resonances in photoionization cross sections do not appear for a relatively large energy range. The cross section σ_{PI} of the ground level has smooth background with prominent resonances belonging to $n = 2$ thresholds. In Figures 7 and 8 the first resonance complex LL ($2l2l$) is easily identifiable and is followed by Ln' ($n' > 2$) resonances converging onto $n = 2$ thresholds of the core. In contrast to the ground level, the excited levels show a K-shell jump at the $n = 2$ threshold due to the $1s$–$2p$ transition:

$$h\nu + \text{N VI/F VIII}(1s2s,\ 1s2p) \rightarrow e + \text{N VII/F IX}(2s,\ 2p),$$

as seen in Figures 7*b*–7*e* and 8*b*–8*e*.

Similar to the excited levels of N V (Fig. 3), all excited levels of N VI and F VIII show the existence of PEC resonances in the photoionization cross sections.

4.2.2. *Electron-Ion Recombination*

The total electron-ion recombination collision strength (Ω_{RC}) and total cross sections (σ_{RC}) are obtained for the recombined He-like ions N VI and F VIII. Both quantities have similar features. Only σ_{RC} is presented in the top panel of Figure 9 for N VI and of Figure 10 for F VIII. The total unified photorecombination cross section σ_{RC} corresponds to the summed contributions from the low-n photorecombination cross sections of all levels, as well as the high-n DR cross sections. The cross section σ_{RC} diverges at zero photoelectron energy (eq. [8]), but decays smoothly with energy until resonance complexes appear at very high energies. The Rydberg series of resonances form LL, LM, etc., complexes that converge onto the $n = 2$ thresholds; MM, MN, etc., complexes that converge onto the $n = 3$ thresholds; and NN, NO, etc., complexes that converge onto the $n = 4$ thresholds. LL denotes the series $2l2l'$, LM denotes $2l3l'$, etc. Some of the complexes are marked in the figures. The resonances become much weaker and narrower beyond the $n = 2$ thresholds.

The velocity-dependent photorecombination rates [$\alpha_{RC}(E) = v\sigma_{RC}(E)$] for N VI and F VIII are obtained for energies up to the $n = 4$ thresholds of the respective core ions. The bottom panels of Figures 9 and 10 present the resonant part of $\alpha_{RC}(E)$ below the $n = 2$ thresholds, as the higher resonant complexes are much weaker. As mentioned before, $\langle v\alpha_{RC}\rangle$ is a measurable quantity in experiments. It is measured as convolved over the monochromatic bandwidth of the beam.

Total unified recombination rate coefficients for N VI and F VIII are presented for a wide range of temperatures, $1 \leq \log_{10} T \leq 9$. The rates are tabulated in Table 4, and the features are illustrated and compared with the available rates in Figures 11*a* and 11*b*. The BPRM unified coefficients $\alpha_R(T)$ (*solid curves*) show the basic features. The recombination rate coefficient starts high at very low temperature due to the dominance of RR into an infinite

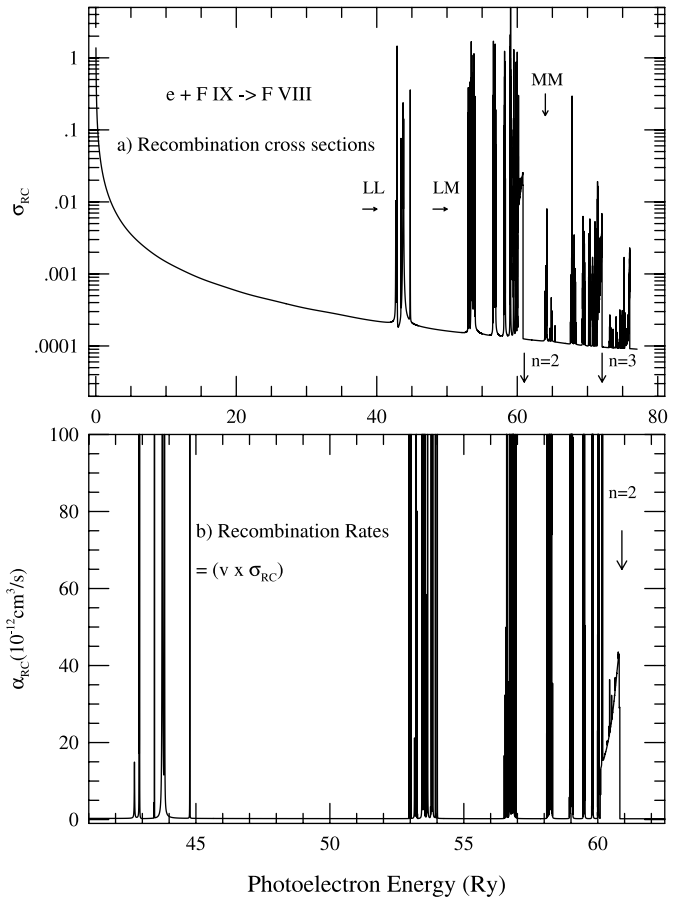

FIG. 10.—(*a*) Total unified (e + ion) recombination cross sections, $\sigma_{\rm RC}$, and (*b*) unified recombination rate coefficients, $\alpha_{\rm RC}(E)$, vs. photoelectron energy for (e + F IX → F VIII). Note the separated resonance complexes LL, LM, etc., of the $n = 2$; MM, MN, etc., of the $n = 3$; and NN, etc., of the $n = 4$ thresholds. The coefficient $\alpha_{\rm RC}(E)$, convolved with an energy bandwidth, is a measurable quantity.

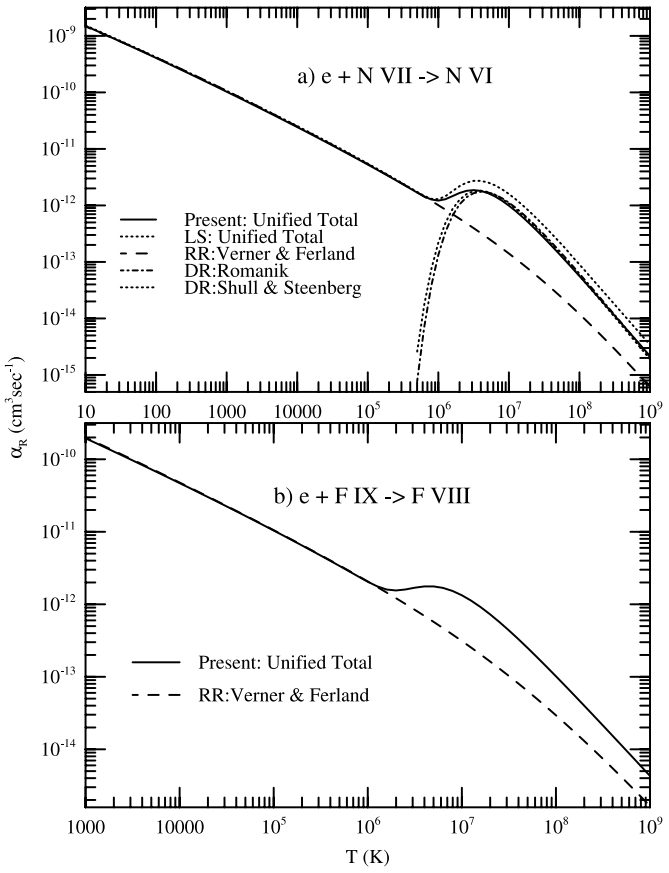

FIG. 11.—Total unified recombination rate coefficients $\alpha_R(T)$ (*solid curves*) for (*a*) N VI and (*b*) F VIII. The RR rates are from Verner & Ferland (1996; *dashed curves*). For N VI, the total unified rate in *LS* coupling is from Nahar & Pradhan (1997; *dotted curve*), and the DR rates are from Romanik (1988; *dot-dashed curve*) and Shull & Steenberg (1982; *short-dashed–long-dashed curve*).

number of high-n levels, decreases with increasing temperature until high T, where it forms a "bump" due to the dominant DR process, and follows to a smooth decay due to damping of recombination cross sections by the exponential of the Maxwellian electron distribution.

The present BPRM total unified recombination rate coefficients $\alpha_R(T)$ for N VI and F VIII compare very well with the RR rate coefficients by Verner & Ferland (1996; *dashed curves*). For N VI, the DR peak is lower than that of the earlier *LS* coupling unified rate (Nahar & Pradhan 1997). The reason is the radiation damping of autoionizing resonances included in the present calculations. The high-temperature peak agrees very well with the fit to DR rates by Shull & Steenberg (1982; *short-dashed–long-dashed curve*) and by Romanik (1988; *dot-dashed curve*). They obtained the DR rates using isolated resonance approximations, which can give accurate DR rates when the interference between DR and RR, such as for these ions, is negligible. There is no DR rate for F VII available for comparison.

Level-specific recombination rate coefficients are presented for all 172 levels of N VI and 178 levels of F VIII. They correspond to $n(SLJ)$ with $0 \leq J \leq 10$ and $n \leq 10$. Table 6 presents level-specific recombination rates for the ground and $n = 2$ levels corresponding to the X-ray w, x, y, and z lines of N VI and F VIII. The rates show a relatively smooth decay with temperature and a small shoulder at high temperature due to DR resonances.

5. CONCLUSION

Extensive results from the relativistic BPRM calculations for total and level-specific photoionization and recombination cross sections and rate coefficients are presented for Li- and He-like N V, F VII, N VI, and F VIII for UV and X-ray spectroscopy of laboratory and astrophysical sources. The unified method for (electron+ion) recombination explicitly provides level-specific recombination rates and self-consistent photoionization cross sections of hundreds of bound levels. The level-specific data are obtained for the first time. The present data are expected to be of high accuracy based on the very good agreement of the energies with the experimental values, inclusion of atomic effects such as relativistic effects, radiation damping of resonances, and channel couplings, and accuracy of the method. Comparison of the recombination cross sections and rates obtained using the unified method for ions such as carbon and oxygen (Zhang et al. 1999) with those measured experimentally showed agreement within 10%–15%. Similar accuracy is expected for all He- and Li-like ions being studied. The present data are more than sufficient for the extrapolation to high n, l necessary to account for all recombination-cascade contributions.

Total recombination rate coefficients are presented at a wide temperature range for all practical applications. With featureless hydrogenic behavior at lower temperatures, the recombination rates of these few electron systems show isoelectronic z-dependency. Similar to the rate of a hydrogenic ion, which varies as $z\alpha_R(H, T/z^2)$, the rate increases with higher ionic charge. The resonances are not z-dependent, except that they get narrower

TABLE 6

LEVEL-SPECIFIC RECOMBINATION RATE COEFFICIENTS FOR THE GROUND AND Kα LEVELS OF N VI AND F VIII

$\log_{10} T$ (K)	α_R(cm^3 s^{-1})				
	$1s^2\ {}^1S_0$	$1s2s^3S_1$	$1s2p^3P^o_1$	$1s2p^1P^o_1$	$1s2p^3P^o_2$
	N VI				
	BE = −40.5	−9.72	−9.24	−8.91	−9.24
1.0	1.16E−10	2.17E−11	2.13E−11	1.79E−11	3.55E−11
1.1	1.04E−10	1.93E−11	1.90E−11	1.59E−11	3.16E−11
1.2	9.25E−11	1.72E−11	1.69E−11	1.42E−11	2.82E−11
1.3	8.24E−11	1.53E−11	1.51E−11	1.26E−11	2.51E−11
1.4	7.35E−11	1.37E−11	1.35E−11	1.13E−11	2.24E−11
1.5	6.55E−11	1.22E−11	1.20E−11	1.00E−11	2.00E−11
1.6	5.83E−11	1.09E−11	1.07E−11	8.95E−12	1.78E−11
1.7	5.20E−11	9.68E−12	9.52E−12	7.98E−12	1.58E−11
1.8	4.63E−11	8.62E−12	8.49E−12	7.11E−12	1.41E−11
1.9	4.13E−11	7.69E−12	7.56E−12	6.34E−12	1.26E−11
2.0	3.68E−11	6.85E−12	6.74E−12	5.65E−12	1.12E−11
2.1	3.28E−11	6.11E−12	6.01E−12	5.03E−12	1.00E−11
2.2	2.92E−11	5.44E−12	5.36E−12	4.49E−12	8.91E−12
2.3	2.61E−11	4.85E−12	4.77E−12	4.00E−12	7.94E−12
2.4	2.32E−11	4.32E−12	4.25E−12	3.56E−12	7.08E−12
2.5	2.07E−11	3.85E−12	3.79E−12	3.18E−12	6.31E−12
2.6	1.85E−11	3.43E−12	3.38E−12	2.83E−12	5.62E−12
2.7	1.64E−11	3.06E−12	3.01E−12	2.52E−12	5.01E−12
2.8	1.47E−11	2.73E−12	2.68E−12	2.25E−12	4.46E−12
2.9	1.31E−11	2.43E−12	2.39E−12	2.00E−12	3.98E−12
3.0	1.16E−11	2.17E−12	2.13E−12	1.79E−12	3.55E−12
3.1	1.04E−11	1.93E−12	1.90E−12	1.59E−12	3.16E−12
3.2	9.25E−12	1.72E−12	1.69E−12	1.42E−12	2.82E−12
3.3	8.24E−12	1.53E−12	1.51E−12	1.26E−12	2.51E−12
3.4	7.34E−12	1.37E−12	1.34E−12	1.13E−12	2.23E−12
3.5	6.55E−12	1.22E−12	1.20E−12	1.00E−12	1.99E−12
3.6	5.83E−12	1.09E−12	1.07E−12	8.93E−13	1.77E−12
3.7	5.20E−12	9.68E−13	9.49E−13	7.95E−13	1.58E−12
3.8	4.63E−12	8.63E−13	8.45E−13	7.08E−13	1.41E−12
3.9	4.13E−12	7.69E−13	7.53E−13	6.30E−13	1.25E−12
4.0	3.68E−12	6.85E−13	6.70E−13	5.61E−13	1.11E−12
4.1	3.28E−12	6.11E−13	5.96E−13	4.99E−13	9.92E−13
4.2	2.92E−12	5.45E−13	5.30E−13	4.43E−13	8.82E−13
4.3	2.60E−12	4.85E−13	4.71E−13	3.94E−13	7.84E−13
4.4	2.32E−12	4.33E−13	4.19E−13	3.50E−13	6.97E−13
4.5	2.07E−12	3.86E−13	3.72E−13	3.10E−13	6.18E−13
4.6	1.84E−12	3.44E−13	3.29E−13	2.75E−13	5.48E−13
4.7	1.64E−12	3.07E−13	2.92E−13	2.43E−13	4.86E−13
4.8	1.46E−12	2.73E−13	2.58E−13	2.15E−13	4.29E−13
4.9	1.30E−12	2.44E−13	2.28E−13	1.89E−13	3.79E−13
5.0	1.16E−12	2.17E−13	2.01E−13	1.66E−13	3.34E−13
5.1	1.03E−12	1.94E−13	1.76E−13	1.46E−13	2.93E−13
5.2	9.19E−13	1.73E−13	1.54E−13	1.27E−13	2.57E−13
5.3	8.17E−13	1.54E−13	1.35E−13	1.10E−13	2.24E−13
5.4	7.26E−13	1.37E−13	1.17E−13	9.53E−14	1.94E−13
5.5	6.44E−13	1.22E−13	1.01E−13	8.19E−14	1.68E−13
5.6	5.71E−13	1.09E−13	8.68E−14	7.00E−14	1.44E−13
5.7	5.06E−13	9.74E−14	7.41E−14	6.00E−14	1.23E−13
5.8	4.47E−13	8.90E−14	6.29E−14	5.34E−14	1.05E−13
5.9	3.95E−13	8.53E−14	5.30E−14	5.20E−14	8.82E−14
6.0	3.48E−13	8.71E−14	4.45E−14	5.72E−14	7.40E−14
6.1	3.05E−13	9.35E−14	3.72E−14	6.77E−14	6.18E−14
6.2	2.67E−13	1.01E−13	3.11E−14	7.99E−14	5.16E−14
6.3	2.33E−13	1.07E−13	2.59E−14	8.96E−14	4.29E−14
6.4	2.02E−13	1.08E−13	2.16E−14	9.38E−14	3.55E−14
6.5	1.74E−13	1.04E−13	1.78E−14	9.18E−14	2.92E−14
6.6	1.49E−13	9.51E−14	1.46E−14	8.47E−14	2.38E−14
6.7	1.26E−13	8.34E−14	1.18E−14	7.43E−14	1.92E−14
6.8	1.06E−13	7.06E−14	9.42E−15	6.25E−14	1.53E−14
6.9	8.89E−14	5.80E−14	7.44E−15	5.09E−14	1.20E−14

TABLE 6—*Continued*

$\log_{10} T$ (K)	α_R(cm^3 s^{-1})				
	$1s^2\ {}^1S_0$	$1s2s^3S_1$	$1s2p^3P^o_1$	$1s2p^1P^o_1$	$1s2p^3P^o_2$
	N VI				
	BE = −40.5	−9.72	−9.24	−8.91	−9.24
7.0	7.37E−14	4.65E−14	5.81E−15	4.03E−14	9.39E−15
7.1	6.05E−14	3.65E−14	4.50E−15	3.12E−14	7.26E−15
7.2	4.93E−14	2.83E−14	3.45E−15	2.38E−14	5.57E−15
7.3	3.99E−14	2.16E−14	2.63E−15	1.79E−14	4.24E−15
7.4	3.20E−14	1.64E−14	1.99E−15	1.33E−14	3.21E−15
7.5	2.55E−14	1.23E−14	1.50E−15	9.78E−15	2.42E−15
7.6	2.02E−14	9.16E−15	1.13E−15	7.16E−15	1.82E−15
7.7	1.59E−14	6.80E−15	8.42E−16	5.21E−15	1.36E−15
7.8	1.24E−14	5.03E−15	6.27E−16	3.77E−15	1.01E−15
7.9	9.62E−15	3.70E−15	4.66E−16	2.72E−15	7.54E−16
8.0	7.44E−15	2.72E−15	3.46E−16	1.96E−15	5.60E−16
8.1	5.72E−15	2.00E−15	2.56E−16	1.41E−15	4.14E−16
8.2	4.38E−15	1.46E−15	1.89E−16	1.01E−15	3.06E−16
8.3	3.34E−15	1.07E−15	1.39E−16	7.23E−16	2.26E−16
8.4	2.53E−15	7.79E−16	1.02E−16	5.17E−16	1.66E−16
8.5	1.92E−15	5.67E−16	7.52E−17	3.70E−16	1.22E−16
8.6	1.44E−15	4.13E−16	5.52E−17	2.64E−16	8.97E−17
8.7	1.09E−15	3.00E−16	4.04E−17	1.89E−16	6.58E−17
8.8	8.13E−16	2.18E−16	2.96E−17	1.35E−16	4.82E−17
8.9	6.08E−16	1.58E−16	2.16E−17	9.60E−17	3.52E−17
9.0	4.53E−16	1.15E−16	1.58E−17	6.84E−17	2.58E−17
	F VIII				
	BE = −70.1	−17.0	−16.3	−15.9	−16.3
1.0	1.98E−10	3.83E−11	3.70E−11	3.21E−11	6.15E−11
1.1	1.77E−10	3.41E−11	3.30E−11	2.86E−11	5.48E−11
1.2	1.58E−10	3.04E−11	2.94E−11	2.55E−11	4.89E−11
1.3	1.40E−10	2.71E−11	2.62E−11	2.27E−11	4.36E−11
1.4	1.25E−10	2.41E−11	2.34E−11	2.03E−11	3.88E−11
1.5	1.12E−10	2.15E−11	2.08E−11	1.81E−11	3.46E−11
1.6	9.95E−11	1.92E−11	1.86E−11	1.61E−11	3.08E−11
1.7	8.86E−11	1.71E−11	1.65E−11	1.43E−11	2.75E−11
1.8	7.90E−11	1.52E−11	1.47E−11	1.28E−11	2.45E−11
1.9	7.04E−11	1.36E−11	1.31E−11	1.14E−11	2.18E−11
2.0	6.28E−11	1.21E−11	1.17E−11	1.02E−11	1.95E−11
2.1	5.59E−11	1.08E−11	1.04E−11	9.05E−12	1.73E−11
2.2	4.98E−11	9.61E−12	9.30E−12	8.07E−12	1.55E−11
2.3	4.44E−11	8.56E−12	8.29E−12	7.19E−12	1.38E−11
2.4	3.96E−11	7.63E−12	7.39E−12	6.41E−12	1.23E−11
2.5	3.53E−11	6.80E−12	6.58E−12	5.71E−12	1.09E−11
2.6	3.15E−11	6.06E−12	5.87E−12	5.09E−12	9.75E−12
2.7	2.80E−11	5.40E−12	5.23E−12	4.54E−12	8.69E−12
2.8	2.50E−11	4.82E−12	4.66E−12	4.04E−12	7.75E−12
2.9	2.23E−11	4.29E−12	4.15E−12	3.60E−12	6.90E−12
3.0	1.98E−11	3.83E−12	3.70E−12	3.21E−12	6.15E−12
3.1	1.77E−11	3.41E−12	3.30E−12	2.86E−12	5.48E−12
3.2	1.58E−11	3.04E−12	2.94E−12	2.55E−12	4.89E−12
3.3	1.40E−11	2.71E−12	2.62E−12	2.27E−12	4.35E−12
3.4	1.25E−11	2.41E−12	2.33E−12	2.02E−12	3.88E−12
3.5	1.12E−11	2.15E−12	2.08E−12	1.80E−12	3.46E−12
3.6	9.94E−12	1.92E−12	1.85E−12	1.61E−12	3.08E−12
3.7	8.86E−12	1.71E−12	1.65E−12	1.43E−12	2.74E−12
3.8	7.90E−12	1.52E−12	1.47E−12	1.27E−12	2.44E−12
3.9	7.04E−12	1.36E−12	1.31E−12	1.14E−12	2.18E−12
4.0	6.27E−12	1.21E−12	1.17E−12	1.01E−12	1.94E−12
4.1	5.59E−12	1.08E−12	1.04E−12	9.00E−13	1.73E−12
4.2	4.98E−12	9.61E−13	9.24E−13	8.01E−13	1.54E−12
4.3	4.44E−12	8.57E−13	8.23E−13	7.12E−13	1.37E−12
4.4	3.95E−12	7.63E−13	7.32E−13	6.34E−13	1.22E−12
4.5	3.52E−12	6.80E−13	6.51E−13	5.63E−13	1.08E−12

TABLE 6—*Continued*

$\log_{10} T$ (K)	α_R(cm^3 s^{-1})				
	$1s^2\ {}^1S_0$	$1s2s^3S_1$	$1s2p^3P^o_1$	$1s2p^1P^o_1$	$1s2p^3P^o_2$
	F VIII				
	BE = −70.1	−17.0	−16.3	−15.9	−16.3
4.6	3.14E−12	6.06E−13	5.78E−13	5.00E−13	9.61E−13
4.7	2.79E−12	5.41E−13	5.13E−13	4.44E−13	8.53E−13
4.8	2.49E−12	4.82E−13	4.55E−13	3.93E−13	7.57E−13
4.9	2.22E−12	4.29E−13	4.03E−13	3.48E−13	6.71E−13
5.0	1.97E−12	3.83E−13	3.57E−13	3.08E−13	5.93E−13
5.1	1.76E−12	3.41E−13	3.15E−13	2.71E−13	5.24E−13
5.2	1.56E−12	3.04E−13	2.78E−13	2.39E−13	4.62E−13
5.3	1.39E−12	2.71E−13	2.44E−13	2.09E−13	4.06E−13
5.4	1.24E−12	2.41E−13	2.14E−13	1.83E−13	3.56E−13
5.5	1.10E−12	2.15E−13	1.87E−13	1.60E−13	3.11E−13
5.6	9.77E−13	1.91E−13	1.63E−13	1.38E−13	2.71E−13
5.7	8.67E−13	1.70E−13	1.41E−13	1.19E−13	2.34E−13
5.8	7.69E−13	1.52E−13	1.21E−13	1.02E−13	2.02E−13
5.9	6.81E−13	1.35E−13	1.04E−13	8.79E−14	1.73E−13
6.0	6.02E−13	1.23E−13	8.84E−14	7.77E−14	1.47E−13
6.1	5.31E−13	1.17E−13	7.48E−14	7.44E−14	1.25E−13
6.2	4.68E−13	1.18E−13	6.31E−14	7.98E−14	1.05E−13
6.3	4.10E−13	1.25E−13	5.32E−14	9.27E−14	8.94E−14
6.4	3.59E−13	1.34E−13	4.49E−14	1.08E−13	7.63E−14
6.5	3.13E−13	1.40E−13	3.79E−14	1.21E−13	6.54E−14
6.6	2.71E−13	1.40E−13	3.20E−14	1.27E−13	5.59E−14
6.7	2.34E−13	1.34E−13	2.67E−14	1.24E−13	4.74E−14
6.8	2.00E−13	1.22E−13	2.21E−14	1.15E−13	3.96E−14
6.9	1.70E−13	1.07E−13	1.81E−14	1.01E−13	3.27E−14
7.0	1.44E−13	9.05E−14	1.46E−14	8.54E−14	2.65E−14
7.1	1.21E−13	7.43E−14	1.16E−14	6.96E−14	2.11E−14
7.2	1.00E−13	5.96E−14	9.07E−15	5.53E−14	1.66E−14
7.3	8.26E−14	4.69E−14	7.03E−15	4.29E−14	1.29E−14
7.4	6.75E−14	3.64E−14	5.41E−15	3.27E−14	9.91E−15
7.5	5.47E−14	2.78E−14	4.12E−15	2.46E−14	7.55E−15
7.6	4.40E−14	2.11E−14	3.12E−15	1.83E−14	5.71E−15
7.7	3.52E−14	1.59E−14	2.35E−15	1.35E−14	4.29E−15
7.8	2.79E−14	1.19E−14	1.76E−15	9.88E−15	3.21E−15
7.9	2.20E−14	8.85E−15	1.32E−15	7.20E−15	2.39E−15
8.0	1.72E−14	6.56E−15	9.79E−16	5.22E−15	1.77E−15
8.1	1.34E−14	4.85E−15	7.27E−16	3.77E−15	1.31E−15
8.2	1.04E−14	3.57E−15	5.38E−16	2.71E−15	9.70E−16
8.3	7.99E−15	2.63E−15	3.97E−16	1.95E−15	7.15E−16
8.4	6.12E−15	1.93E−15	2.93E−16	1.40E−15	5.25E−16
8.5	4.68E−15	1.41E−15	2.16E−16	1.00E−15	3.86E−16
8.6	3.55E−15	1.03E−15	1.58E−16	7.18E−16	2.83E−16
8.7	2.69E−15	7.55E−16	1.16E−16	5.14E−16	2.07E−16
8.8	2.03E−15	5.51E−16	8.52E−17	3.67E−16	1.51E−16
8.9	1.53E−15	4.01E−16	6.24E−17	2.62E−16	1.11E−16
9.0	1.15E−15	2.92E−16	4.56E−17	1.87E−16	8.07E−17

NOTE.—BE is the binding energy of the level in rydbergs.

with higher charge. Hence the z-dependent isoelectronic behavior is not seen at high temperatures where the DR starts contributing. The present $\alpha_{RC}(T)$ agree very well with available total (RR+DR) rates. However, significant differences are noted at the high-T recombination rates where DR is dominant for N V.

The complete set of data includes (1) photoionization cross sections, both total and partial, for bound fine-structure levels of N V–VI and F VII–VIII up to $n = 10$, (2) total unified recombination rate coefficients and level-specific recombination rate coefficients for levels up to $n = 10$ for a wide temperature range, and (3) total unified recombination cross sections and velocity-averaged recombination rate coefficients as functions of the photoelectron energy for comparison with experiments.

All photoionization and recombination data are available electronically from the author.

This work was supported partially by the NASA Astrophysical Theory Program and the Space Astrophysical Research and Analysis programs. The computational work was carried out at the Ohio Supercomputer Center in Columbus, Ohio.

REFERENCES

Bell, R. H., & Seaton, M. J. 1985, J. Phys. B, 18, 1589
Berrington, K. A., Burke, P. G., Butler, K., Seaton, M. J., Storey, P. J., Taylor, K. T., & Yan, Y. 1987, J. Phys. B, 20, 6379
Berrington, K. A., Eissner, W., & Norrington, P. H. 1995, Comput. Phys. Commun., 92, 290
Canizares, C. R., et al. 2000, in Atomic Data Needs for X-Ray Astronomy, ed. M. A. Bautista, T. R. Kallman, & A. K. Pradhan (NASA CP-2000-209968; Greenbelt: NASA), http://heasarc.gsfc.nasa.gov/docs/heasarc/atomic/proceed.html
Dopita, M. A., & Sutherland, R. S. 2003, Astrophysics of the Diffuse Universe (Berlin: Springer)
Eissner, W., Jones, M., & Nussbaumer, H. 1974, Comput. Phys. Commun., 8, 270
Fitzpatrick, E. L., & Spitzer, L., Jr. 1997, ApJ, 475, 623
Gabriel, A. H. 1972, MNRAS, 160, 99
Gabriel, A. H., & Jordan, C. 1969, Nature, 221, 947
Hillier, J. 2005, A Study of Epsilon Canis Majoris (B2 II) (*Chandra* Proposal 07200982; Cambridge: CXO)
Hummer, D. G., Berrington, K. A., Eissner, W., Pradhan, A. K., Saraph, H. E., & Tully, J. A. 1993, A&A, 279, 298
Lee, J. C., Ogle, P. M., Canizares, C. R., Marshall, H. L., Schulz, N. S., Morales, R., Fabian, A. C., & Iwasawa, K. 2001, ApJ, 554, L13
Leighly, K. M., O'Brien, P. T., Edelson, R., George, I. M., Malkan, M. A., Matsuoka, M., Mushotzky, R. F., & Peterson, B. M. 1997, ApJ, 483, 767
Nahar, S. N. 1996, Phys. Rev. A, 53, 2417
———. 2002, A&A, 389, 716
Nahar, S. N. 2005, ApJS, 158, 80
Nahar, S. N., Eissner, W., Chen, G.-X., & Pradhan, A. K. 2003, A&A, 408, 789
Nahar, S. N., & Pradhan, A. K. 1992, Phys. Rev. Lett., 68, 1488
———. 1994, Phys. Rev. A, 49, 1816
———. 1997, ApJS, 111, 339
———. 2000, Phys. Scr., 61, 675
———. 2003, ApJS, 149, 239
———. 2006, ApJS, 162, 417
Nahar, S. N., Pradhan, A. K., & Zhang, H. L. 2000, ApJS, 131, 375
———. 2001, ApJS, 133, 255
Ness, J.-U., Brickhouse, N. S., Drake, J. J., & Huenemoerder, D. P. 2003, ApJ, 598, 1277
Oelgoetz, J., & Pradhan, A. K. 2001, MNRAS, 327, L42
———. 2004, MNRAS, 354, 1093
Pradhan, A. K., Chen, G.-X., Nahar, S. N., & Zhang, H. L. 2001, Phys. Rev. Lett., 87, 183201
Pradhan, A. K., & Zhang, H. L. 1997, J. Phys. B, 30, L571
Romanik, C. 1988, ApJ, 330, 1022
Sakimoto, K., Terao, M., & Berrington, K. A. 1990, Phys. Rev. A, 42, 291
Scott, N. S., & Burke, P. G. 1980, J. Phys. B, 13, 4299
Scott, N. S., & Taylor, K. T. 1982, Comput. Phys. Commun., 25, 347
Shull, J. M., & van Steenberg, M. 1982, ApJS, 48, 95
Verner, D. A., & Ferland, G. 1996, ApJS, 103, 467
Zhang, H. L., Nahar, S. N., & Pradhan, A. K. 1999, J. Phys. B, 32, 1459